

1
2
3
4
5
6
7
8
9
10
11
12
13

Calibration and Uncertainty Quantification of Convective Parameters in an Idealized GCM

Oliver R. A. Dunbar¹, Alfredo Garbuno-Inigo², Tapio Schneider¹,
Andrew M. Stuart¹

¹California Institute of Technology, Pasadena, California, USA
²Instituto Tecnológico Autónomo de México, Ciudad de México, México.

Key Points:

- We use time averaged climate statistics to calibrate convective parameters and quantify their uncertainties.
- We demonstrate use of the calibrate-emulate-sample algorithm to provide efficient calibration and uncertainty quantification.
- The algorithm leverages ensemble simulations, over convective parameters, to quantify parametric uncertainties in climate predictions.

Corresponding author: Oliver Dunbar, odunbar@caltech.edu

14 **Abstract**

15 Parameters in climate models are usually calibrated manually, exploiting only small sub-
 16 sets of the available data. This precludes an optimal calibration and quantification of
 17 uncertainties. Traditional Bayesian calibration methods that allow uncertainty quantifi-
 18 cation are too expensive for climate models; they are also not robust in the presence of
 19 internal climate variability. For example, Markov chain Monte Carlo (MCMC) methods
 20 typically require $O(10^5)$ model runs, rendering them infeasible for climate models. Here
 21 we demonstrate an approach to model calibration and uncertainty quantification that
 22 requires only $O(10^2)$ model runs and can accommodate internal climate variability. The
 23 approach consists of three stages: (i) a calibration stage uses variants of ensemble Kalman
 24 inversion to calibrate a model by minimizing mismatches between model and data statis-
 25 tics; (ii) an emulation stage emulates the parameter-to-data map with Gaussian processes
 26 (GP), using the model runs in the calibration stage for training; (iii) a sampling stage
 27 approximates the Bayesian posterior distributions by using the GP emulator and then
 28 samples using MCMC. We demonstrate the feasibility and computational efficiency of
 29 this calibrate-emulate-sample (CES) approach in a perfect-model setting. Using an ide-
 30 alized general circulation model, we estimate parameters in a simple convection scheme
 31 from data surrogates generated with the model. The CES approach generates probabil-
 32 ity distributions of the parameters that are good approximations of the Bayesian pos-
 33 teriors, at a fraction of the computational cost usually required to obtain them. Sam-
 34 pling from this approximate posterior allows the generation of climate predictions with
 35 quantified parametric uncertainties.

36 **Plain Language Summary**

37 Calibrating climate models with available data and quantifying their uncertainties
 38 is essential to make climate predictions accurate and actionable. A primary source of un-
 39 certainties in climate models comes from representation of small-scale processes such as
 40 moist convection. Parameters in these convection schemes and other parameterizations
 41 are usually calibrated by hand, using only a small fraction of data that are available. As
 42 a result, the calibration process may miss information about the small-scale processes
 43 in question. This paper presents a proof-of-concept, in an idealized setting, of how pa-
 44 rameters in climate models can be calibrated using a substantial fraction of the avail-
 45 able data, and uncertainties in the parameters can be quantified. We employ a new al-
 46 gorithm, called calibrate-emulate-sample (CES), which makes such calibration and un-
 47 certainty quantification feasible for computationally expensive climate models. CES re-
 48 duces the hundreds of thousands of model runs usually required to quantify uncertain-
 49 ties in computer models to hundred, thereby achieving about a factor 1000 speedup. It
 50 leads to more robust calibration and uncertainty quantification in the presence of noise
 51 arising from chaotic variability of the climate system. We show how uncertainties in cli-
 52 mate model parameters can be translated into quantified uncertainties of climate pre-
 53 dictions through ensemble integrations.

54 **1 Introduction**

55 The principal uncertainties in climate predictions arise from the representation of
 56 unresolvable yet important small-scale processes, such as those controlling cloud cover
 57 (Cess et al., 1989, 1990; Bony & Dufresne, 2005; Stephens, 2005; Bony et al., 2006; Vial
 58 et al., 2013; Webb et al., 2013; Brient & Schneider, 2016; Schneider, Teixeira, et al., 2017).
 59 These processes are represented by parameterization schemes, which relate unresolved
 60 quantities such as cloud statistics to variables resolved on the climate models' compu-
 61 tational grid, such as temperature and humidity. The parameterization schemes depend
 62 on parameters that are a priori unknown, and so fixing the parameters is associated with
 63 uncertainty. The process of fixing these parameters to values that are most consistent

64 with observational data is known as calibration, and requires solving an optimization prob-
65 lem. Traditionally, parameters are calibrated (“tuned”) by hand, in a process that ex-
66 ploits only a small subset of the available observational data and relies on the knowledge
67 and intuition of climate modelers about plausible ranges of parameters and their effect
68 on the simulated climate of a model (Randall & Wielicki, 1997; Mauritsen et al., 2012;
69 Golaz et al., 2013; Hourdin et al., 2013; Flato et al., 2013; Hourdin et al., 2017; Schmidt
70 et al., 2017; Zhao et al., 2018). More recently, some broader-scale automated approaches
71 that more systematically quantify the plausible range of parameters have begun to be
72 explored (Couvreur et al., 2020; Hourdin et al., 2020). However, to fully account for para-
73 metric uncertainty, we require a Bayesian view of the model-data relationship, where model
74 parameters are treated as realizations sampled from an underlying probability distribu-
75 tion. The process of finding the probability distribution of parameters that is most con-
76 sistent with the the observed data is known as uncertainty quantification, and requires
77 solving a Bayesian inverse problem.

78 Opportunities to improve climate models lie in exploiting a larger fraction of the
79 available observational data together with high-resolution simulations, and learning from
80 both systematically and not manually (Schneider, Lan, et al., 2017). Here we provide
81 a relatively simple proof-of-concept of how parameterizations in a climate model can be
82 calibrated and their parametric uncertainties be quantified by minimizing the mismatch
83 between climate statistics simulated with the model and those obtained from observa-
84 tions or high-resolution simulations. We focus on learning from time-averaged climate
85 statistics for three reasons: (1) time-averaged statistics are what is relevant for climate
86 predictions; (2) time-averaged statistics vary more smoothly in space than atmospheric
87 states, leading to a smoother optimization problem than that of atmospheric state es-
88 timation in numerical weather prediction (NWP); (3) time-averaging over long time-intervals
89 reduces the effect of the unknown initial state of the system, removing the need to de-
90 termine it. Focusing on time-averaged climate statistics, rather than on instantaneous
91 states or trajectories as in NWP, makes it possible to exploit climate observations and
92 high-resolution simulations even when their native resolutions are very different from those
93 of climate models.

94 While learning from climate statistics accumulated in time presents opportunities,
95 it also comes with challenges. Accumulating statistics in time is computationally much
96 more expensive than the forecasts over hours or days used in NWP. Therefore, we need
97 algorithms for learning from data that are fast, requiring a minimum of climate model
98 runs. Traditional methods for Bayesian calibration and uncertainty quantification such
99 as Markov chain Monte Carlo (MCMC) typically require many iterations—often more
100 than 10^5 —to reach statistical convergence (see (Geyer, 2011) for an overview). Conduct-
101 ing so many computationally expensive climate model runs is not feasible, rendering MCMC
102 impractical for climate model calibration (Annan & Hargreaves, 2007). Additionally, while
103 MCMC can be used to obtain the distribution of model parameters given data, it is not
104 robust with respect to noise in the evaluation of the map from model parameters to data.
105 Such noise, arising from natural variability in the chaotic climate system, can lead to trap-
106 ping of the Markov chains in spurious, noise-induced local maxima of the likelihood func-
107 tion (Cleary et al., 2021). This presents additional challenges to using MCMC methods
108 for climate model calibration.

109 Here we showcase a new approach to climate model uncertainty quantification that
110 overcomes the limitations of traditional Bayesian calibration methods. The approach—
111 called calibrate-emulate-sample (CES) (Cleary et al., 2021)—consists of three successive
112 stages, which each exploit proven concepts and methods:

- 113 1. In a calibration stage, we use variants of ensemble Kalman inversion, which has
114 proven to be a fast, derivative-free method for state estimation in NWP (Houtekamer
115 & Zhang, 2016), as well as for the solution of inverse problems where the objec-

116 tive is parameter rather than state estimation (Chen & Oliver, 2012a; Emerick &
 117 Reynolds, 2013b; Evensen, 2018; Iglesias et al., 2013). Ensemble methods scale
 118 well to high-dimensional state and parameter spaces, typically with $O(10^2)$ for-
 119 ward model runs (Kalnay, 2003; Oliver et al., 2008). However, ensemble Kalman
 120 methods do not provide a basis for systematic uncertainty quantification, except
 121 in linear problems (Annan & Hargreaves, 2007; Gland et al., 2009; Ernst et al.,
 122 2015).

- 123 2. In an emulation stage, we train an emulator on the climate model statistics gen-
 124 erated during the calibration stage. To emulate how the climate model statistics
 125 depend on parameters to be calibrated, we use Gaussian processes (GPs), a ma-
 126 chine learning method that learns smooth functions and uncertainty about the func-
 127 tions from a set of training points (Kennedy & O’Hagan, 2001; Santner et al., 2018).
 128 The training points here are provided by the climate model runs performed in the
 129 calibration stage.
- 130 3. In a sampling stage, we approximate the posterior distribution on parameters given
 131 data, using the GP emulator to replace the parameter-to-climate statistics map,
 132 and then use MCMC to sample the approximate posterior. Because the GP em-
 133 ulator is computationally cheap to evaluate and is smooth by virtue of the smooth-
 134 ing properties of GPs, this avoids the issues that limit the usability of MCMC for
 135 sampling from climate models directly.

136 The CES approach is described in detail in Cleary et al. (2021), which provides a jus-
 137 tification and contextualization of the approach in the literature on data assimilation and
 138 Bayesian calibration. The purpose of this paper is to demonstrate the feasibility of the
 139 approach for estimating parameters in an idealized general circulation model (GCM).
 140 This represents a proof-of-concept in a small parameter space and limited data space;
 141 how the methods scale up to larger problems will be discussed at the end.

142 This paper is arranged as follows: Section 2 describes the experimental setup, in-
 143 cluding the idealized GCM and the generation of synthetic data from it. Section 3 de-
 144 scribes the CES approach and the methods used in each stage. Section 4 describes the
 145 results of numerical experiments that use CES to calibrate parameters in the idealized
 146 GCM and quantify their uncertainties. It also demonstrates how sampling from the pos-
 147 terior distribution of parameters can be used to generate climate predictions with quan-
 148 tified uncertainties. Section 5 discusses and summarizes the results and their applica-
 149 bility to larger problems.

150 2 Experimental Setup

151 2.1 General Circulation Model

152 We use the idealized GCM described by Frierson et al. (2006) and O’Gorman and
 153 Schneider (2008b), which is based on the spectral dynamical core of the Flexible Mod-
 154 eling System developed at the Geophysical Fluid Dynamics Laboratory. To approximate
 155 the solution of the hydrostatic primitive equations, it uses the spectral transform method
 156 in the horizontal, with spectral resolution T21 and 32 latitude points on the transform
 157 grid. It uses finite differences with 10 unevenly spaced sigma levels in the vertical. We
 158 chose this relatively coarse resolution to keep our numerical experiments computationally
 159 efficient, so that comparison of CES with much more expensive methods is feasible.
 160 The lower boundary of the GCM is a homogeneous slab ocean (1 m mixed-layer thick-
 161 ness). Radiative transfer is represented by a semi-gray, two-stream radiative transfer scheme,
 162 in which the optical depth of longwave and shortwave absorbers is a prescribed function
 163 of latitude and pressure (O’Gorman & Schneider, 2008b), irrespective of the concentra-
 164 tion of water vapor in the atmosphere (i.e., without an explicit representation of water
 165 vapor feedback). Insolation is constant and approximates Earth’s annual mean insola-
 166 tion at the top of the atmosphere.

We focus our calibration and uncertainty quantification experiments on parameters in the GCM’s convection scheme, which is a quasi-equilibrium moist convection scheme that can be viewed as a simplified version of the Betts-Miller convection scheme (Betts, 1986; Betts & Miller, 1986, 1993). It relaxes temperature T and specific humidity q toward reference profiles on a timescale τ (Frierson, 2007):

$$\frac{\partial T}{\partial t} + \dots = -f_T \frac{T - T_{\text{ref}}}{\tau} \quad (1)$$

and

$$\frac{\partial q}{\partial t} + \dots = -f_T f_q \frac{q - q_{\text{ref}}}{\tau}. \quad (2)$$

167 Here, $f_T(z; T, q, p)$ is a function of altitude z and of the thermodynamic state of an at-
 168 mospheric column (dependent on temperature T , pressure p , and specific humidity q in
 169 the column), which determines where and when the convection scheme is active; $f_q(T, q, p)$
 170 is a function that modulates the relaxation of the specific humidity in non-precipitating
 171 (shallow) convection (Frierson, 2007; O’Gorman & Schneider, 2008b). The reference tem-
 172 perature profile is a moist adiabat, $T_{\text{ma}}(z)$, shifted by a state-dependent and constant-
 173 with-height offset ΔT , which is chosen to ensure conservation of enthalpy integrated over
 174 a column: $T_{\text{ref}}(z) = T_{\text{ma}}(z) + \Delta T$. The reference specific humidity $q_{\text{ref}}(z)$ is the spe-
 175 cific humidity corresponding to a fixed relative humidity RH relative to the moist adi-
 176 abat $T_{\text{ma}}(z)$. The two key parameters in this simple convection scheme thus are the timescale
 177 τ and the relative humidity RH; we demonstrate how we can learn about them from syn-
 178 thetic data generated with the GCM.

179 2.2 Variable Selection and Generation of Synthetic Data

180 The idealized GCM with the simple quasi-equilibrium convection scheme has been
 181 used in numerous studies of large-scale atmosphere dynamics and mechanisms of climate
 182 changes, especially those involving the hydrologic cycle (e.g., O’Gorman & Schneider,
 183 2008b, 2008a; Bordoni & Schneider, 2008; O’Gorman & Schneider, 2009b; Schneider et
 184 al., 2010; Merlis & Schneider, 2011; O’Gorman, 2011; Kaspi & Schneider, 2011, 2013; Levine
 185 & Schneider, 2015; Bischoff & Schneider, 2014; Wills et al., 2017; Wei & Bordoni, 2018).
 186 We know from this body of work that the convection scheme primarily affects the at-
 187 mospheric thermal stratification in the tropics, with weaker effects in the extratropics
 188 (Schneider & O’Gorman, 2008). We also know that the relative humidity parameter (RH)
 189 in the moist convection scheme controls the humidity of the tropical free troposphere but
 190 likewise has a weaker effect on the humidity of the extratropical free troposphere (O’Gorman
 191 et al., 2011). Thus, we expect tropical circulation statistics to be especially informative
 192 about the parameters in the convection scheme. However, convection plays a central role
 193 in extreme precipitation events at all latitudes (O’Gorman & Schneider, 2009b, 2009a),
 194 so we expect statistics of precipitation extremes to be informative about convective pa-
 195 rameters, and in particular to contain information about the relaxation timescale τ .

196 As the climate statistics from which we want to learn about the convective param-
 197 eters, we choose 30-day averages of the free-tropospheric relative humidity, of the pre-
 198 cipitation rate, and of a measure of the frequency of extreme precipitation. Because the
 199 GCM is statistically zonally symmetric, we take zonal averages in addition to the time
 200 averages. The relative humidity is evaluated at $\sigma = 0.5$ (where $\sigma = p/p_s$ is pressure
 201 p normalized by the local surface pressure p_s), as shown in Figure 1. As a measure of
 202 the frequency of precipitation extremes, we use the probability that daily precipitation
 203 rates exceed a high, latitude-dependent threshold. The threshold is chosen as the latitude-
 204 dependent 90th percentile of daily precipitation in a long (18000 days) control simula-
 205 tion of the GCM in a statistically steady state. So for the parameters in the control sim-
 206 ulation, the precipitation threshold is expected to be exceeded 10% of the time at each
 207 latitude. The convective parameters in the control simulation are fixed at their reference
 208 values $\text{RH} = 0.7$ and $\tau = 2$ h (O’Gorman & Schneider, 2008b), and we collect the pa-
 209 rameters in the vector $\theta^\dagger = (\theta_{\text{RH}}^\dagger, \theta_\tau^\dagger) = (0.7, 2 \text{ h})$. Figure 2 shows the mean relative

210 humidity, the mean precipitation rate (broken down into its contributions coming from
 211 the convection scheme and from condensation at resolved scales), and the 90th percentile
 212 precipitation rate, from the control simulation averaged over 600 batches of 30-day win-
 213 dows. We use the single long control simulations of duration 18000 days only for the crea-
 214 tion of Figure 2 and for the estimation of noise covariances, described next.

215 2.3 Definition of noise covariance

216 Estimation of model parameters requires specification of a noise covariance matrix,
 217 reflecting errors and uncertainties in the data. The principal source of noise in our perfect-
 218 model setting with synthetic data is sampling variability due to finite-time averaging with
 219 unknown initial conditions. The initial condition is forgotten at sufficiently long times
 220 because of the chaotic nature of atmospheric variability, so a central limit theorem quan-
 221 tifies the finite-time fluctuations around infinite-time averages that are caused by uncer-
 222 tain initial conditions. Therefore, the asymptotic distribution of the fluctuations is a mul-
 223 tivariate normal distribution $N(0, \Sigma(\theta))$ with zero mean and covariance matrix $\Sigma(\theta)$. We
 224 estimate the covariance matrix at $\Sigma(\theta^\dagger)$, that is, with the parameters θ^\dagger in the control
 225 simulation. To estimate $\Sigma(\theta^\dagger)$, we run the GCM for 600 windows of length 30 days (be-
 226 cause we use 30-day averages to estimate parameters) and calculate the sample covari-
 227 ance matrix. With the 3 latitude-dependent fields evaluated at 32 latitude points, $\Sigma(\theta^\dagger)$
 228 is a 96×96 symmetric matrix representing noise from internal variability in finite-time
 229 averages. Hereafter, we make the assumption that $\Sigma(\theta) \approx \Sigma(\theta^\dagger)$ for any θ , and thus
 230 we treat Σ as a constant matrix.

To generate our surrogate data, we also include the effect of measurement error (Kennedy
 & O’Hagan, 2001). We add Gaussian noise to the time-averaged model statistics, with
 a diagonal covariance structure in data space. We construct the measurement error co-
 variance matrix Δ to be diagonal with entries $\delta_i > 0$, where i indexes over data type
 (the 3 observed quantities) and latitude (32 locations). Combining this measurement co-
 variance matrix Δ with the covariance matrix Σ arising from internal variability leads
 to an inflated noise covariance matrix

$$\Gamma = \Sigma + \text{diag}(\delta_i) = \Sigma + \Delta, \quad (3)$$

There are many options to pick δ_i . We choose it by reducing a distance of the 95% con-
 fidence interval to its nearest physical boundary for each i by a constant factor C , which
 retains physical properties e.g., precipitation must be nonnegative. Denote the mean μ_i ,
 variance Σ_{ii} , and a physical boundary set $\partial\Omega_i$ for each data i , we choose

$$\delta_i = C \min \left(\text{dist}(\mu_i + 2\sqrt{\Sigma_{ii}}, \partial\Omega_i), \text{dist}(\mu_i - 2\sqrt{\Sigma_{ii}}, \partial\Omega_i) \right).$$

231 We take $C = 0.2$. This value implies a significant noise inflation, with the average rati-
 232 o of standard deviations $\sqrt{\Gamma_{ii}}/\sqrt{\Sigma_{ii}}$ being 2.3. In Figure 3, we display the resulting data
 233 mean (grey circles), the 95% confidence interval of the inflated covariance (grey ribbon),
 234 and four realizations of the truth $\mathbf{y}^{(1)}, \dots, \mathbf{y}^{(4)}$ (yellow to red lines), each defined by tak-
 235 ing a different 30-day average of the GCM, and adding a different realization of $N(0, \Delta)$.
 236 These four realizations will be used throughout when presenting our results.

237 3 Methods

238 3.1 Objective functions for time averaged data

239 Both calibration and uncertainty quantification in CES rely on an objective func-
 240 tion (standardized error) that quantifies mismatch between model output and data. Cal-
 241 ibration minimizes the objective function over the parameter space, and the same ob-
 242 jective function is the negative log-likelihood of the posterior distribution which is sam-
 243 pled to perform uncertainty quantification. To define the desired objective function, we

244 introduce $\mathcal{G}_T(\boldsymbol{\theta}; \mathbf{z}^{(0)})$ and $\mathcal{G}_\infty(\boldsymbol{\theta})$, which denote the mapping from the parameter vec-
 245 tor $\boldsymbol{\theta}$ to the 96 data points, either averaged over a finite time horizon (T) or over an in-
 246 finite time horizon (∞). The former average depends on the unknown initial condition
 247 $\mathbf{z}^{(0)}$, whereas the latter does not, because the initial condition is forgotten after a suf-
 248 ficiently long time. We refer to $\mathcal{G}_T(\boldsymbol{\theta}; \mathbf{z}^{(0)})$ as the forward model and $\mathcal{G}_\infty(\boldsymbol{\theta})$ as the in-
 249 finite time-horizon forward model.

To define the objective function, we begin from the relationship between param-
 eters $\boldsymbol{\theta}$ and data \mathbf{y} . Expressed in terms of finite-time averages, this relationship has the
 form

$$\mathbf{y} = \mathcal{G}_T(\boldsymbol{\theta}; \mathbf{z}^{(0)}) + N(0, \Delta). \quad (4)$$

This form has the undesirable feature that it involves $\mathbf{z}^{(0)}$, a quantity which is not of in-
 trinsic interest. We note that, invoking the central limit theorem, which quantifies the
 forgetting of the initial condition after long times, we may also write

$$\mathbf{y} = \mathcal{G}_\infty(\boldsymbol{\theta}) + N(0, \Gamma). \quad (5)$$

250 This removes the dependence on initial condition but is expressed in terms of infinite-
 251 time averages. Computing these averages directly is not feasible, but we introduce a pro-
 252 cedure that enables us to learn a surrogate model for their computation, using carefully
 253 chosen finite-time averages.

In the Bayesian approach to parameter learning, the aim is to determine the con-
 ditional distribution of parameters $\boldsymbol{\theta}$ given data \mathbf{y} , assuming the relationship (5) between
 $\boldsymbol{\theta}$ and \mathbf{y} , together with prior information on $\boldsymbol{\theta}$. This leads to introduction of the objec-
 tive function (negative log-likelihood)

$$\Phi(\boldsymbol{\theta}) = \frac{1}{2} \|\mathbf{y} - \mathcal{G}_\infty(\boldsymbol{\theta})\|_\Gamma^2, \quad (6)$$

where $\|\cdot\|_\Gamma = \|\Gamma^{-1/2} \cdot\|_2$ is the Mahalanobis distance. Before a surrogate model for
 \mathcal{G}_∞ is available, this function is infeasible to evaluate, but we may consider the related
 objective function

$$\Phi_T(\boldsymbol{\theta}; \mathbf{z}^{(0)}) = \frac{1}{2} \|\mathbf{y} - \mathcal{G}_T(\boldsymbol{\theta}; \mathbf{z}^{(0)})\|_{\Gamma+\Sigma}^2. \quad (7)$$

254 Here we view evaluation of \mathcal{G}_T from any initial condition as a random approximation of
 255 \mathcal{G}_∞ , hence the additional internal-variability covariance matrix Σ appearing in (7).

256 Our broad intent is as follows: to use optimization based on (7) to calibrate pa-
 257 rameters; on the basis of evaluations of \mathcal{G}_T made during this calibration, to learn a GP
 258 surrogate for \mathcal{G}_∞ ; then utilize this surrogate to sample from the posterior distribution
 259 of $(\boldsymbol{\theta} | \mathbf{y})$ defined using (6). To this end, we will henceforth neglect $\mathbf{z}^{(0)}$ in our nota-
 260 tion, and just write $\mathcal{G}_T(\boldsymbol{\theta})$ and $\Phi_T(\boldsymbol{\theta})$. Dropping the dependence of the initial condition
 261 from these objects makes evaluations of them non-deterministic.

262 We have the following undesirable properties of the finite-time model average $\mathcal{G}_T(\boldsymbol{\theta})$:
 263 (i) it is computationally expensive to evaluate for large T ; (ii) it can be nondifferentiable
 264 or difficult to differentiate (e.g., because of non-differentiability of parameterization schemes
 265 in climate models); and (iii) evaluations of it are not deterministic (when one drops the
 266 explicit dependence on initial conditions). Our methodology, detailed in the upcoming
 267 sections, is constructed to overcome these difficulties.

268 3.2 Calibrate: Ensemble Kalman Inversion

269 Ensemble Kalman inversion (EKI) (Iglesias et al., 2013) is an offline variant of en-
 270 semble Kalman filtering designed to learn parameters in a general model, rather than
 271 states of a dynamical system. EKI can be viewed as a derivative-free optimization al-
 272 gorithm. Given a set of data \mathbf{y} , it iteratively evolves an ensemble of parameter estimates

273 both so that they achieve consensus and evolve toward the optimal parameter value θ^*
 274 (likely close to θ^\dagger) that minimizes the objective (7), possibly with inclusion of a regu-
 275 larization term. It has great potential for use with chaotic or stochastic models due to
 276 its ensemble-based, derivative-free approach for optimizing parameters. Furthermore, the
 277 derivative-free approach scales well to high-dimensional parameter spaces, as evidenced
 278 by the use of Kalman filtering in numerical weather prediction, where billions of param-
 279 eters characterizing atmospheric states are routinely estimated (Kalnay, 2002). This makes
 280 the algorithm appealing for complex climate models. The algorithm is mathematically
 281 proven to find the optimizer, within an initial, ensemble-dependent subspace, for linear
 282 models (Schillings & Stuart, 2017), and it is known to be effective for high-dimensional
 283 nonlinear models (Iglesias et al., 2013; Schneider et al., 2020b, 2020a), such as the non-
 284 linear map from parameters to data represented by the idealized GCM we use in our proof-
 285 of-concept here.

The EKI algorithm we use is detailed in (Iglesias et al., 2013). The algorithm it-
 eratively updates an ensemble of parameters, $\theta_m^{(n)}$, where $m = 1, \dots, M$ denotes an en-
 semble member, and the superscript n denotes the iteration count. The algorithm uses
 the ensemble to update parameters according to the following equation

$$\theta_m^{(n+1)} = \theta_m^{(n)} + C_{\theta\mathcal{G}}^{(n)} \left((\Gamma + \Sigma) + C_{\mathcal{G}\mathcal{G}}^{(n)} \right)^{-1} \left(\mathbf{y} - \mathcal{G}_T(\theta_m^{(n)}) \right),$$

286 where $C_{\mathcal{G}\mathcal{G}}$ is the empirical covariance of the ensemble of quantities of interest from model
 287 runs, and $C_{\theta\mathcal{G}}$ is the empirical cross-covariance of the ensemble of parameters and the
 288 ensemble of quantities of interest. The noise distribution of the difference in realizations
 289 of \mathbf{y} and $\mathcal{G}_T(\cdot)$ is $\Gamma + \Sigma$. Often, EKI is implemented with additional independent noise
 290 added to \mathbf{y} at each iteration and for each ensemble member. However, because the in-
 291 dividual evaluations of $\mathcal{G}_T(\cdot)$ are affected by internal variability, here we omit use of this
 292 additional noise.

293 We initialize the algorithm by drawing an ensemble of size $M = 100$ by sampling
 294 the parameter space from assumed prior distributions on the parameters. The priors are
 295 taken to be the logit-normal and lognormal distributions, $\theta_{RH} \sim \text{Logit}[N(0, 1)]$ and $\theta_\tau \sim$
 296 $\text{Log}[N(12 \text{ h}, (12 \text{ h})^2)]$, for the relative humidity and timescale parameter, respectively.
 297 This choice allows us to apply our methods in a transformed space (by applying the logit
 298 and log transformations, respectively), where the priors are normally distributed and un-
 299 bounded; meanwhile the climate model works with untransformed variables, which are
 300 bounded within $[0, 1]$ and $[0, \infty)$, respectively. Thus, the prior distributions enforce phys-
 301 ical constraints on the parameters.

302 3.3 Emulate: Gaussian Process Emulators (EKI-GP)

During the calibration stage with N iterations and ensemble of size M , we obtain
 a collection of input–output pairs

$$\{\theta_m^{(n)}, \mathcal{G}_T(\theta_m^{(n)})\}, \quad n = 0, \dots, N, \quad m = 1, \dots, M.$$

303 The cloud of points $\{\theta_m^{(n)}\}$ from an EKI run will span the initial draws of the prior dis-
 304 tribution, but with a high density around the point θ^* to which EKI eventually converges.
 305 We use regression to train a GP emulator mapping θ to $\mathcal{G}_T(\theta)$, using the input–output
 306 pairs $\{\theta_m^{(n)}, \mathcal{G}_T(\theta_m^{(n)})\}$, which are referred to as training points in the context of GP re-
 307 gression. The emulation will be most accurate in regions with more training points, that
 308 is, around θ^* . This is typically near the true solution θ^\dagger , and it is the region where the
 309 posterior parameter distribution will have high probability; this is precisely where un-
 310 certainty quantification requires accuracy. In effect, EKI serves as an effective algorithm
 311 for selecting good training points for GP regression.

Gaussian processes emulate the statistics of the input–output pairs, using a Gaussian assumption. Specifically, we learn an approximation of the form

$$\mathcal{G}_T(\boldsymbol{\theta}) \approx \mathcal{N}(\mathcal{G}_{\text{GP}}(\boldsymbol{\theta}), \Sigma_{\text{GP}}(\boldsymbol{\theta})).$$

312 The approximation is learned from the input–output pairs assuming that the outputs are
 313 produced from a mean function $\mathcal{G}_{\text{GP}}(\boldsymbol{\theta})$, and subject to normally distributed noise defined
 314 by a covariance function $\Sigma_{\text{GP}}(\boldsymbol{\theta})$, both dependent on the parameters. The choice
 315 of notation here is to imply the fact that $\mathcal{G}_{\text{GP}}(\boldsymbol{\theta})$ serves to approximate the (unattainable)
 316 infinite-time average of the model $\mathcal{G}_{\infty}(\boldsymbol{\theta})$, and $\Sigma_{\text{GP}}(\boldsymbol{\theta})$ serves to approximate the
 317 covariance matrix Σ . Importantly, $\Sigma_{\text{GP}}(\boldsymbol{\theta})$ is $\boldsymbol{\theta}$ -dependent as it also includes the uncertainty
 318 in approximation of the emulator at $\boldsymbol{\theta}$ (for example, the emulator uncertainty $\Sigma_{\text{GP}}(\boldsymbol{\theta})$
 319 will be large when $\boldsymbol{\theta}$ is far from the inputs $\{\boldsymbol{\theta}_m\}$ used in training).

The atmospheric quantities from which we learn about model parameters are correlated (e.g., relative humidity or daily precipitation at neighboring latitudes are correlated), resulting in a nondiagonal covariance matrix Σ . Any GP emulator therefore also requires a nondiagonal covariance $\Sigma_{\text{GP}}(\boldsymbol{\theta})$. We can enforce this, by (i) mapping the correlated statistics from the GCM into a decorrelated space by using a principal component analysis on Σ , and then (ii) train the GP with the decorrelated statistics to produce an emulator with diagonal covariance $\tilde{\Sigma}_{\text{GP}}(\boldsymbol{\theta})$. We use the notation $(\tilde{\cdot})$ to denote variables in the uncorrelated space. To this end, we first decompose Σ as

$$\Sigma = VD^2V^T.$$

Here, V is an orthonormal matrix of eigenvectors of the covariance matrix Σ , and D is the diagonal matrix of the square root of the eigenvalues, or the ordered standard deviations in the basis spanned by the eigenvectors of Σ . We store the outputs from the pairs as columns of a matrix $Y_{kl} = (\mathcal{G}_T(\boldsymbol{\theta}_l))_k$, then we change the basis of this matrix into the uncorrelated coordinates

$$\tilde{Y} = D^{-1}V^TY.$$

320 When trained on \tilde{Y} , the GP returns $\tilde{\mathcal{G}}_{\text{GP}}(\boldsymbol{\theta})$ and (diagonal) $\tilde{\Sigma}_{\text{GP}}(\boldsymbol{\theta})$. We use tools from
 321 scikit-learn (Pedregosa et al., 2011) to train the emulator. After the diagonalization, we
 322 can train a scalar-valued GP for each of the 96 output dimensions, rather than having
 323 to train processes with vector-valued output. We construct a kernel by summing an Automatic Relevance Determination (ARD) radial basis function kernel and a white-noise kernel. This corresponds to regression, rather than interpolation, and the variance of the white noise kernel reflects the noise level assumed in the regression. We then require the training of 4 hyperparameters: the radial basis function variance, a lengthscale for each of the two parameters $\boldsymbol{\theta}$ (due to ARD), and the white-noise variance. We train using the input–output pairs of the initial ensemble plus $N = 5$ subsequent iterations of the EKI algorithm. We use $M = 100$ ensemble members; thus, the training requires $(N + 1) \times M = 600$ 30-day runs of our GCM.
 331

332 We continue using the uncorrelated basis in the sampling stage, but if required, one
 333 can always transform the output of the emulator back into a correlated basis,

$$\begin{aligned} \mathcal{G}_{\text{GP}}(\boldsymbol{\theta}) &= VD\tilde{\mathcal{G}}_{\text{GP}}(\boldsymbol{\theta}), \\ \Sigma_{\text{GP}}(\boldsymbol{\theta}) &= VD\tilde{\Sigma}_{\text{GP}}(\boldsymbol{\theta})DV^T. \end{aligned}$$

334 3.4 Sample: MCMC Sampling with a Gaussian Process Emulator

335 To quantify uncertainties, we use MCMC to sample the posterior distribution of
 336 parameters with the GP emulator. The primary reason for using the GP emulator goes
 337 back to the seminal paper by Sacks et al. (1989) and concerns the fact that it can be evaluated far more quickly than the GCM at a point in parameter space; this is important
 338

339 as we require more than 10^5 samples within the likelihood $\mathbb{P}(\mathbf{y} | \boldsymbol{\theta})$ in a typical MCMC
 340 run to sample the posterior distribution of parameters given data. However the emula-
 341 tor is also important for two additional reasons: (i) it naturally includes the approxima-
 342 tion uncertainty (within $\tilde{\Sigma}_{\text{GP}}$) of using an emulator; (ii) it smooths the likelihood func-
 343 tion because we work with an approximation of (6) based on the smooth \mathcal{G}_{∞} , rather than
 344 (7) based on the noisy \mathcal{G}_T ; as a result, MCMC is less likely to get stuck in local extrema.

Recall that we trained the GP in uncorrelated coordinates. Within MCMC, one can either map back into the original coordinates or continue working in the uncorrelated space. We choose to continue working in the uncorrelated space, and so we map each data realization \mathbf{y} into this space: $\tilde{\mathbf{y}} = D^{-1}V^T\mathbf{y}$. In the Gaussian likelihood, we can use the GP emulated mean $\tilde{\mathcal{G}}_{\text{GP}}(\boldsymbol{\theta})$ and covariance matrix $\tilde{\Sigma}_{\text{GP}}(\boldsymbol{\theta})$ as surrogates for the map \mathcal{G}_{∞} and the internal variability covariance matrix Σ (after passing to the uncorrelated coordinates). That is, we approximate the Bayesian posterior distribution as

$$\begin{aligned} \mathbb{P}(\boldsymbol{\theta} | \tilde{\mathbf{y}}) &\propto \mathbb{P}(\tilde{\mathbf{y}} | \boldsymbol{\theta})\mathbb{P}(\boldsymbol{\theta}) \\ &\propto \frac{1}{\sqrt{\det(\tilde{\Gamma}_{\text{GP}}(\boldsymbol{\theta}))}} \exp\left(-\frac{1}{2}\|\tilde{\mathbf{y}} - \tilde{\mathcal{G}}_{\text{GP}}(\boldsymbol{\theta})\|_{\tilde{\Gamma}_{\text{GP}}(\boldsymbol{\theta})}^2\right) \mathbb{P}(\boldsymbol{\theta}) \\ &\propto \exp\left(-\frac{1}{2}\|\tilde{\mathbf{y}} - \tilde{\mathcal{G}}_{\text{GP}}(\boldsymbol{\theta})\|_{\tilde{\Gamma}_{\text{GP}}(\boldsymbol{\theta})}^2 - \frac{1}{2}\log \det \tilde{\Gamma}_{\text{GP}}(\boldsymbol{\theta})\right) \mathbb{P}(\boldsymbol{\theta}). \end{aligned}$$

345 Here, $\tilde{\Gamma}_{\text{GP}}(\boldsymbol{\theta}) = \tilde{\Sigma}_{\text{GP}}(\boldsymbol{\theta}) + D^{-1}V^T\Delta VD^{-1}$ is the GP approximation of $\Gamma = \Sigma + \Delta$ in
 346 the uncorrelated coordinates. We include the (often overlooked) log-determinant term,
 347 arising from the normalization constant due to dependence of Γ_{GP} on $\boldsymbol{\theta}$. In the trans-
 348 formed parameter space, our prior $\mathbb{P}(\boldsymbol{\theta})$ is also Gaussian and therefore can be factored
 349 inside this exponential, adding a quadratic penalty to the objective function (negative
 350 log posterior). The resulting objective function is smooth and suitable for use within an
 351 MCMC algorithm to generate samples from the approximate posterior distribution of
 352 the parameters. Cleary et al. (2021) contains further discussion of MCMC using GPs
 353 to emulate the forward model, including situations where data comes from finite time-
 354 averages but the emulator is designed to approximate the infinite time-horizon forward
 355 model.

356 We use the random walk metropolis algorithm for MCMC sampling. The priors
 357 chosen were the same, physics-informed priors used to initialize EKI. We choose the pro-
 358 posal distribution also as a Gaussian with covariance proportional to the prior covari-
 359 ance. The MCMC run consists of a burn-in of 10,000 samples followed by 190,000 sam-
 360 ples.

361 3.5 Benchmark Gaussian process (B-GP)

362 The performance of any emulator is dependent on the training points. Since we use
 363 an adaptive procedure (EKI) to concentrate the training points, which is the novel ap-
 364 proach introduced in Cleary et al. (2021), we also train a benchmark emulator to com-
 365 pare our results with those resulting from more traditional, brute-force approaches to
 366 the emulation. As a benchmark, we use a GP emulator trained on a uniform set of points.
 367 It is prohibitive to span the entire unbounded prior distributions for this purpose. In-
 368 stead, we use a uniform grid of $40 \times 40 = 1600$ training points to span $[-1.25, -0.5] \times$
 369 $[8.0, 10.0]$ in the transformed parameter space. This corresponds to $[0.62, 0.77] \times [0.83 \text{ h}, 6.12 \text{ h}]$
 370 in the untransformed parameter space and captures the region of high probability of the
 371 posterior. The benchmark emulator uses the same kernel and training setup as in sec-
 372 tion 3.3, and we use the trained emulator in MCMC experiments in the same way as de-
 373 scribed in Section 3.4. To distinguish the two methods, we refer to the EKI-trained GP
 374 as EKI-GP and the benchmark (traditionally trained) GP as B-GP.

375 **4 Results**

376 To demonstrate the dependence of the parameter uncertainty on the realization of
 377 the (inflated) synthetic data, we reproduce the experiments 4 times with each of the four
 378 realizations shown in Figure 3. We denote these four sets of data $\mathbf{y}^{(1)}, \dots, \mathbf{y}^{(4)}$.

379 **4.1 Calibrate: Ensemble Kalman Inversion**

380 We use the first 6 iterations of EKI in the training process for our methodology.
 381 These are shown in Figure 4. The left column displays the full ensemble in parameter
 382 space; the right column zooms in near the true parameter values. The initial ensemble
 383 is spread over the whole parameter space but collapses within a few iterations near the
 384 true parameter values—to within 10% error in θ_{RH} and 30 minutes error in θ_τ . That is,
 385 the algorithm evolves toward consensus and toward the true solution. Biases arise from
 386 the realization of internal variability, and the realization of the observational noise, in
 387 each $\mathbf{y}^{(\cdot)}$.

To check for EKI convergence we evaluate a further 4 iterations of the EKI (labeled
 0 to 9). At each iteration n , we compute residuals of the ensemble mean for each real-
 ization of the synthetic data $\mathbf{y}^{(1)}, \dots, \mathbf{y}^{(4)}$ created at the true parameters θ^\dagger ,

$$\text{Residual}(n; \mathbf{y}^{(i)}) = \left\| \frac{1}{M} \sum_{m=1}^M \mathcal{G}_T(\theta_m^{(n)}) - \mathbf{y}^{(i)} \right\|_\Gamma^2,$$

388 weighting the residuals by the covariance matrix Γ of the synthetic data. Figure 5(a) shows
 389 the residual over EKI iterations. The residual decreases quickly over the first few iter-
 390 ations, before plateauing for subsequent iterations. Figure 5(b) shows standard devia-
 391 tions of the ensemble of parameters. The standard deviations decrease monotonically
 392 from iteration to iteration, reflecting the evolution toward consensus. The behavior is
 393 qualitatively similar for all realizations; quantitative differences reflect different realiza-
 394 tions of internal variability in the different data realizations.

395 **4.2 Emulate: Validation**

396 Figure 6 shows the parameter values used for training points for the EKI-GP and
 397 B-GP. We use the first 6 EKI iterations (i.e., 600 training points) for training. These are
 398 plotted over the associated objective function used in the MCMC. The panels in the left
 399 column correspond to the EKI-GP using truths $\mathbf{y}^{(1)}, \dots, \mathbf{y}^{(4)}$. We see the EKI-GP train-
 400 ing points are well concentrated near the minimum of the objective function; there are
 401 also training points that fall outside of the plotting domain (see Figure 4 for their ext-
 402 ent). The right column of Figure 6 shows the benchmark grid for B-GP, which is not
 403 concentrated and hence samples the posterior distribution inefficiently; the objective func-
 404 tion contours were calculated using the same realization as their counterpart EKI-GPs.
 405 We see that EKI-GP produces qualitatively similar results to those resulting from B-GP;
 406 the quantitative differences are accounted for by differing geometry and number of train-
 407 ing points (and hence a difference in approximation uncertainty). In both settings, the
 408 objective function is smooth because the GP smoothly approximates \mathcal{G}_∞ .

409 EKI-GP shows similar results for the objective function as B-GP, at a fraction of
 410 the computational effort. B-GP is far less practical as a methodology than is EKI-GP
 411 because it does not scale well to high-dimensional parameter spaces; it requires many
 412 more training points than EKI-GP. The B-GP comparison is included simply to demon-
 413 strate that EKI-GP achieves comparable results to those achieved by means of traditional
 414 emulation.

415 We validate the emulator approximation to the data by making a prediction at the
 416 true parameters θ^\dagger . We display $\mathcal{G}_{GP}(\theta^\dagger)$ and the 95% confidence intervals computed us-

417 ing the variance from $\Sigma_{\text{GP}}(\theta^\dagger)$ in Figure 7 for EKI-GP, and in Figure 8 for B-GP. The
 418 rows of Figure 7 correspond to the EKI-GP results for $\mathbf{y}^{(1)}, \dots, \mathbf{y}^{(4)}$. In both figures we
 419 also show the statistics of 600 30-day samples from the control simulation at θ^\dagger . Both
 420 the mean and 95% confidence intervals of all EKI-GP emulators (orange line and rib-
 421 bon) closely match the statistics from the GCM runs (blue dots and error bars), as does
 422 the prediction from the B-GP (dark red line and ribbon). The training data are suffi-
 423 cient to ensure that the predicted 95% confidence interval from the emulators do not pro-
 424 duce unphysical values (such as giving negative precipitation rates, or relative humiditi-
 425 ties outside $[0, 1]$).

426 **4.3 Sample: MCMC Sampling**

427 MCMC algorithms are used to generate a set of samples from the posterior distri-
 428 bution defined using GP emulation. We choose the random walk step size (which mul-
 429 tiples the covariance in the proposal) at the start of a run to achieve proposal acceptance
 430 rates near to 25%. (This is near optimal in a precise sense for certain high-dimensional
 431 posteriors (Roberts et al., 2004); in practice, it works well beyond this setting.) All sam-
 432 pling is performed in the transformed space where the prior distribution is normal. Fig-
 433 ure 9 shows kernel density estimates of the MCMC results; the panels in the left column
 434 are for EKI-GP (for $\mathbf{y}^{(1)}, \dots, \mathbf{y}^{(4)}$), and the panels in the right columns are for B-GP at
 435 the same realizations for the same data. We display contours of the posterior that con-
 436 tain 50%, 75%, and 99% of the mass of the posterior density.

437 All sets of results converge to similar regions of the parameter space about the true
 438 parameters, and the spread of uncertainty is quantified similarly in both EKI-GP and
 439 B-GP. Table 1 shows the standard deviations of the individual parameters alongside the
 440 empirical standard deviation calculated from the ensemble spread in EKI iteration 9. The
 441 standard deviations from the MCMC posterior based on EKI-GP and B-GP are simi-
 442 lar; in contrast, the EKI ensemble spread underestimates the uncertainty in the param-
 443 eters by orders of magnitude. Methods are available to enhance the spread of EKI but
 444 are only justifiable in the Gaussian posterior setting (Chen & Oliver, 2012b; Emerick &
 445 Reynolds, 2013a). Our approach is justifiable whenever the GP accurately approximates
 446 the forward model (Cleary et al., 2021). The use of EKI for the design of training points
 447 for the GP does not require accurate uncertainty quantification within EKI; it only re-
 448 lies on EKI approximately locating minimizers of the model-data misfit objective func-
 449 tion.

450 There is sampling variability due to the different realizations of the truth. This sam-
 451 pling variability can be assessed by asking which probability contours contain the true
 452 parameters. For both EKI-GP and B-GP, in three of four realizations we capture the
 453 true values within 50% of the posterior probability mass; the realization $\mathbf{y}^{(3)}$ is captured
 454 only within the 99% contour of the posterior probability.

455 **4.4 Uncertainty Quantification in Prediction Experiments**

456 To illustrate how the posterior distribution of parameters obtained in the sample
 457 step of the CES algorithm can be used to produce climate predictions with quantified
 458 uncertainties, we consider an idealized global-warming experiment. As in O’Gorman and
 459 Schneider (2008a, 2008b), we rescale the longwave opacity of the atmosphere everywhere
 460 by a uniform factor α . In the control climate we have considered so far, $\alpha = 1$. We gen-
 461 erate a warm climate by setting $\alpha = 1.5$, which results in a global-mean surface air tem-
 462 perature increase from 287 K in the control climate to 294 K in the warm climate. To
 463 see parametric uncertainty rather than internal variability noise in the resulting “climate
 464 change predictions,” we use long (7,200-day or approximately 20-year) averages in the
 465 prediction experiments.

466 We evaluate predictions of the latitude-dependent relative humidity and mean pre-
 467 cipitation rate that we used in the CES algorithm. We also consider the frequency of pre-
 468 cipitation extremes, now taken as the frequency with which the 99.9th percentile of daily
 469 precipitation in the control simulation is exceeded (rather than the 90th percentile we
 470 considered earlier). This last statistic indicates how the frequency of what are 1-in-1000
 471 day precipitation events in the control climate change in the warmer climate.

472 We investigate the effect of parametric uncertainty on predictions by taking 100
 473 samples of parameters from the posterior, create a prediction for each sample, and com-
 474 pare statistics of these runs with runs in which parameters are fixed to the true values
 475 θ^\dagger . The climate statistics in the control climate are shown in the left column of Figure
 476 10. The runs from posterior samples (orange) and with fixed true parameters (blue) match
 477 well. The noise due to internal variability is quantitatively represented by the blue shaded
 478 region. Unlike in the earlier figures with short (30-day) averages (e.g., Figure 8), the in-
 479 ternal variability noise here is small relative to the parametric uncertainty because of the
 480 (long) 7200-day averaging window. The orange shaded region contains both internal vari-
 481 ability and parametric uncertainty and is dominated by parametric uncertainty. This re-
 482 mains the case in the warmer climate (right column of Figure 10).

483 The effects of global warming on atmospheric quantities is seen by comparing the
 484 two columns of Figure 10. Relative humidity is fairly robust to the warming climate, and
 485 precipitation rates increase globally (O’Gorman & Schneider, 2008b). The most dramatic
 486 changes occur for the frequency of extreme precipitation events (O’Gorman & Schnei-
 487 der, 2009b). What is a 1-in-1000 day event in the control climate (e.g., occurring with
 488 frequency 0.001) occurs in the extratropics of the warmer climate an order of magnitude
 489 more frequently, with the 95% confidence interval spanning 0.01 to 0.03. That is, a 1-
 490 in-1000 day event in the control climate occurs every 30 to 100 days in the warmer cli-
 491 mate. The parametric uncertainty is particularly large for extreme precipitation events
 492 within the tropics—behavior one would not be able to see in global warming experiments
 493 with fixed parameters. This is consistent with the known high uncertainty in predictions
 494 of tropical rainfall extremes with comprehensive climate models (O’Gorman & Schnei-
 495 der, 2009a).

496 5 Conclusion and Discussion

497 The primary goal of this article was to demonstrate that ensemble Kalman inver-
 498 sion (EKI), machine learning, and MCMC algorithms can be judiciously combined within
 499 the calibrate-emulate-sample framework to efficiently estimate uncertainty of model pa-
 500 rameters in computationally expensive climate models. We provided a proof-of-concept
 501 in a relatively simple idealized GCM.

502 Our approach is novel because we train a machine learning (GP) emulator using
 503 input-output pairs generated from an EKI algorithm. This methodology has several ad-
 504 vantageous features:

- 505 1. It requires a minimal number of runs of the expensive forward model (typically,
 506 $O(100)$ runs).
- 507 2. It generally finds optimal or nearly optimal parameters even in the presence of in-
 508 ternal variability noise because EKI is robust with respect to such noise.
- 509 3. The resulting GP emulation is naturally most accurate around the (a priori un-
 510 known) optimal parameters because this is where EKI training points concentrate.
- 511 4. MCMC shows robust convergence to the posterior distribution, and allows iden-
 512 tification of the optimal parameters with the maximum of the posterior probabili-
 513 ty, because it utilizes an objective function that is smoothed by GP emulation.

514 The effectiveness of GP depends on the training points, and a user must choose how many
 515 iterations of EKI to use for training (before ensemble collapse). In practice, we find the
 516 GP performance is robust as long as we include the initial iteration of training points
 517 (drawn from the prior) in our training set. The necessity of using the initial ensemble
 518 could be side-stepped by using an ensemble method that does not collapse, such as the
 519 recently introduced ensemble Kalman sampler (EKS) (Garbuno-Inigo et al., 2020).

520 The CES algorithm is efficient, as it addresses two dominant sources of computa-
 521 tional expense. First, poor prior knowledge of model parameters requires blind explo-
 522 ration of a possibly high-dimensional parameter space to find optimal parameters and
 523 thus the region of high posterior probability. The CES framework handles this with an
 524 EKI algorithm, which we show to be successful when using time averaged data from a
 525 chaotic nonlinear model. Second, computing parametric uncertainty with a sampling tech-
 526 nique (such as MCMC) generally requires many (10^5 – 10^6) evaluations of an expensive
 527 forward model. We instead solve a cheap approximate problem by exploiting GP em-
 528 ulators. We train the emulators on relatively few ($O(100)$) intelligently chosen evalua-
 529 tions provided by EKI, which ensures that training points are placed where they are most
 530 needed—near the minimum of the model-data misfit. The training itself introduces neg-
 531 ligible computational cost relative to the running of the forward model, and the com-
 532 putational expense of evaluating the emulator in the sampling step is also negligible. Hence,
 533 the CES framework achieves about a factor 1000 speedup over brute-force MCMC al-
 534 gorithms. Significant efforts to accelerate brute-force MCMC without approximation have
 535 been undertaken (Järvinen et al., 2010; Solonen et al., 2012), and improvements of up
 536 to a factor 5 speedup have been made with adaptive and parallelized Markov chains. How-
 537 ever, these approaches still are considerably more expensive than the CES algorithm.

538 The CES algorithm also has a smoothing property, which is beneficial even in sit-
 539 uations where a forward model is cheap enough to apply a brute-force MCMC. If the for-
 540 ward model exhibits internal variability, the objective function for the sampling algorithm
 541 will contain a data misfit of the form (7), which is non-deterministic because it contains
 542 a finite-time average. Without more sophisticated sampling methods, MCMC algorithms
 543 get stuck in local minima. In the CES algorithm, only EKI uses the functional (7), and
 544 EKI is well suited for this purpose. The GP emulator learns the smooth, noiseless model
 545 \mathcal{G}_∞ (in which internal variability disappears), using evaluations of \mathcal{G}_T (which are affected
 546 by internal variability). Thus, MCMC within the CES algorithm uses the smooth GP
 547 approximation of (6).

548 One might ask why a sampling technique such as MCMC is used, as both EKI and
 549 MCMC algorithms produce uncertainty estimates, through the sample covariance of the
 550 ensemble or the variability from sequential samples, respectively. However, we show that
 551 only the uncertainty of MCMC is suitable for robust statistical inference. In our exper-
 552 iments, the sample covariance of an EKI ensemble underpredicts the standard deviation
 553 of parameters by an order of magnitude. As used here, EKI should be viewed as an op-
 554 timization algorithm and not a sampling algorithm. Adding additional spread to match
 555 the posterior within EKI may be achieved for Gaussian posteriors (Chen & Oliver, 2012b;
 556 Emerick & Reynolds, 2013a) or by means of EKS (Garbuno-Inigo et al., 2020); however,
 557 these methods are not justifiable beyond this Gaussian setting. The MCMC algorithm
 558 with CES, on the other hand, samples from an approximate posterior distribution and
 559 is justifiable beyond the Gaussian posterior setting (Cleary et al., 2021).

560 The MCMC results in this study successfully capture the true parameters and their
 561 uncertainties. The results contain natural biases arising from the use of prior distribu-
 562 tions, internal variability of the climate, and use of a single noisy sample as synthetic
 563 data. Despite the sampling variability and emulator constraints, our MCMC samples were
 564 able to capture the true parameters in a 99% confidence interval in our examples, demon-
 565 strating the potential for use of EKI-trained GP emulators for MCMC sampling. Val-
 566 idation of the emulator in Figure 7 supports the MCMC results even further, as do our

567 comparisons with MCMC using the benchmark emulator (Table 1). The GP emulator
 568 both smooths the objective function and allows us to quantify uncertainty by sampling
 569 from the posterior distribution. However, GPs are limited to moderate-dimensional pa-
 570 rameter spaces, so more scalable emulators may be required in future.

571 An alternative form of constraining parameter uncertainty is history matching, or
 572 precalibration (Vernon et al., 2010; Edwards et al., 2011; Williamson et al., 2013). The
 573 idea complements that of Bayesian uncertainty quantification, where instead of search-
 574 ing for a high probability region of parameter space with respect to data, one rules out
 575 regions of parameter space that are deemed inconsistent with the data. Couvreur et al.
 576 (2020) and Hourdin et al. (2020) recently constrained the parameter space of a param-
 577 eterization scheme by approximating a plausibility function over the parameter space us-
 578 ing a Gaussian process, and then removing “implausible” regions of parameter space where
 579 the plausibility function passes a threshold. This removal process is iterated until the
 580 uncertainty of the emulator is small enough, or the space becomes empty. History match-
 581 ing accomplishes a similar adaptivity task as that performed in the CES algorithm by
 582 EKI. During early stages of history matching, however, one must sample the full param-
 583 eter space with reasonable resolution, and emulator training is required at every itera-
 584 tion to evaluate the plausibility function. In contrast, in the CES algorithm, EKI draws
 585 a modest numbers of samples at every iteration and can work directly with noisy model
 586 evaluations, lowering the computational expense. The output of history matching is a
 587 (possibly empty) “acceptable” set of forward model runs; sampling this set leads to an
 588 upper bound on the prediction uncertainty. The benefit of the CES algorithm is that it
 589 provides samples of the posterior distribution, which lead to full estimates of prediction
 590 uncertainty (see Figure 10). For this reason, history matching has been proposed as a
 591 preprocessing step for Bayesian uncertainty quantification, known as precalibration to
 592 improve priors and assess model validity (Vernon et al., 2010; Edwards et al., 2011). The
 593 CES algorithm targets the Bayesian posterior distributions directly.

594 In the more comprehensive climate modeling settings we target, data will be given
 595 from earth observations and from local high-resolution simulations (Schneider, Lan, et
 596 al., 2017). In these settings, model error leads to deficiencies when comparing model eval-
 597 uations to data, leading to structural biases and additional uncertainty that must be quan-
 598 tified in addition to parameter uncertainty. Structural model errors can be quantified
 599 with a flexible hierarchical Gaussian process regression that learns a non-parametric form
 600 of the model deficiency, as demonstrated in prototype problems in Schneider et al. (2020a).
 601 This approach represents model error in an interpretable fashion, as part of the model
 602 itself, rather than in the data space as pioneered in Kennedy and O’Hagan (2001).

603 The CES framework has potential for both the calibration (as optimal parameters
 604 are given by the calibration stage) and uncertainty quantification (as a posterior distri-
 605 bution is given in the sampling stage) of comprehensive climate models, and other com-
 606 putationally expensive models. It is computationally efficient enough to use data aver-
 607 aged in time (e.g., over seasons), which need to be accumulated over longer model runs.
 608 Time-averaged climate statistics, including mean values and higher-order statistics such
 609 as extreme value statistics, are what typically matters in climate predictions. CES al-
 610 lows us to focus model calibration and uncertainty quantification on such immediately
 611 relevant statistics. Using time averaged statistics also has the advantage that it leads to
 612 smoother, albeit still noisy, objective functions when compared with calibration of cli-
 613 mate models by minimizing mismatches in instantaneous, short-term forecasts (Schneider,
 614 Lan, et al., 2017). The latter approach can improve short-term forecasts but may not
 615 translate into improved climate simulations (Schirber et al., 2013). It also suffers from
 616 the difficulty that model resolution and data resolution may be mismatched. Focusing
 617 on climate statistics, as we did in our proof-of-concept here, circumvents this problem:
 618 time-aggregated climate statistics are varying relatively smoothly in space and, hence,
 619 minimizing mismatches in statistics between models and data does not suffer from the

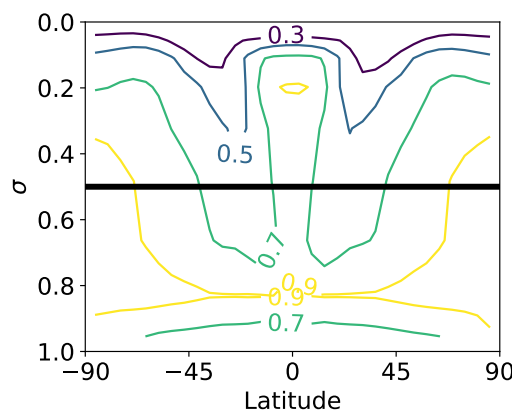


Figure 1. Zonal average of relative humidity averaged over one month. The black line shows the level at which data was extracted for computing objective functions.

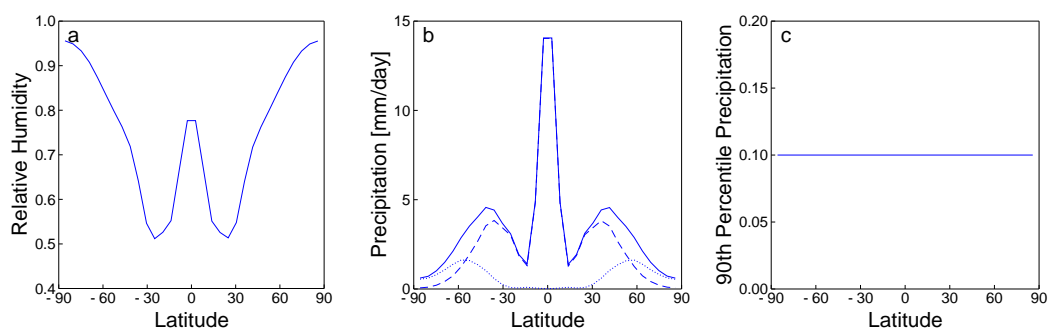


Figure 2. Long-term mean values of the synthetic data. (a) Free-tropospheric relative humidity. (b) Total daily precipitation rate (solid) and its contributions from convection (dashed) and grid-scale condensation (dotted). (c) Probability of daily precipitation exceeding a 90th percentile (which is trivially 10% in this case).

620 resolution-mismatch problem. CES can be used to learn about arbitrary parameters in
 621 climate models from time-averaged data. It leads to quantification of parametric uncer-
 622 tainties that then can be converted into parametric uncertainties in predictions by sam-
 623 pling from the posterior distribution of parameters.

624 Acknowledgments

625 This work was supported by the generosity of Eric and Wendy Schmidt by recommen-
 626 dation of the Schmidt Futures program, by the Hopewell Fund, the Paul G. Allen Fam-
 627 ily Foundation, and the National Science Foundation (NSF, award AGS1835860). A.M.S.
 628 was also supported by the Office of Naval Research (award N00014-17-1-2079). We thank
 629 Emmet Cleary for his preliminary work underlying some of the results shown here.

630 **Data Availability.** All computer code used in this paper is open source. The code for
 631 the idealized GCM, the Julia code for the CES algorithm, the plot tools, and the slurm/bash
 632 scripts to run both GCM and CES are available at <https://doi.org/10.5281/zenodo.4393029>.

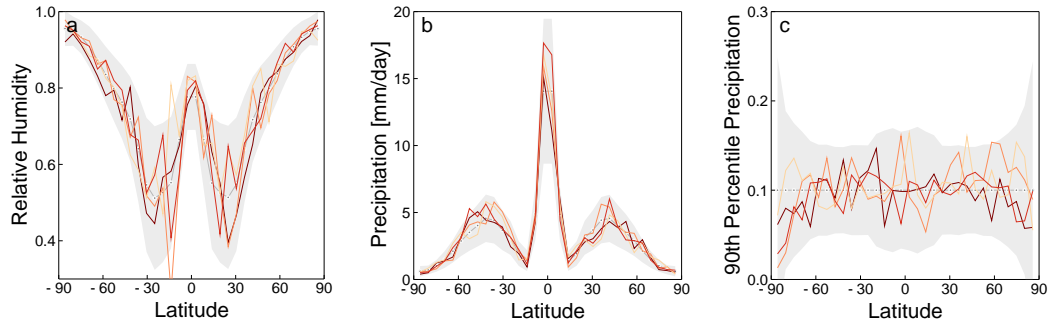


Figure 3. Four noisy realizations of the synthetic data we treat as ‘truth’, plotted in color over the underlying mean (grey circles) and 95% confidence intervals from $\Gamma(\theta^\dagger)$ (grey bars). (a) Relative humidity. (b) Daily precipitation rate. (c) Probability of daily precipitation exceeding the 90th percentile of the long-term mean data.

	σ_{RH}	σ_τ (hrs)
EKI (Iteration 9)	0.017	0.053
MCMC (EKI-GP)	0.099	0.265
MCMC (B-GP)	0.096	0.359

Table 1. Average standard deviations of parameters from EKI and MCMC experiments over $\mathbf{y}^{(1)}, \dots, \mathbf{y}^{(4)}$.

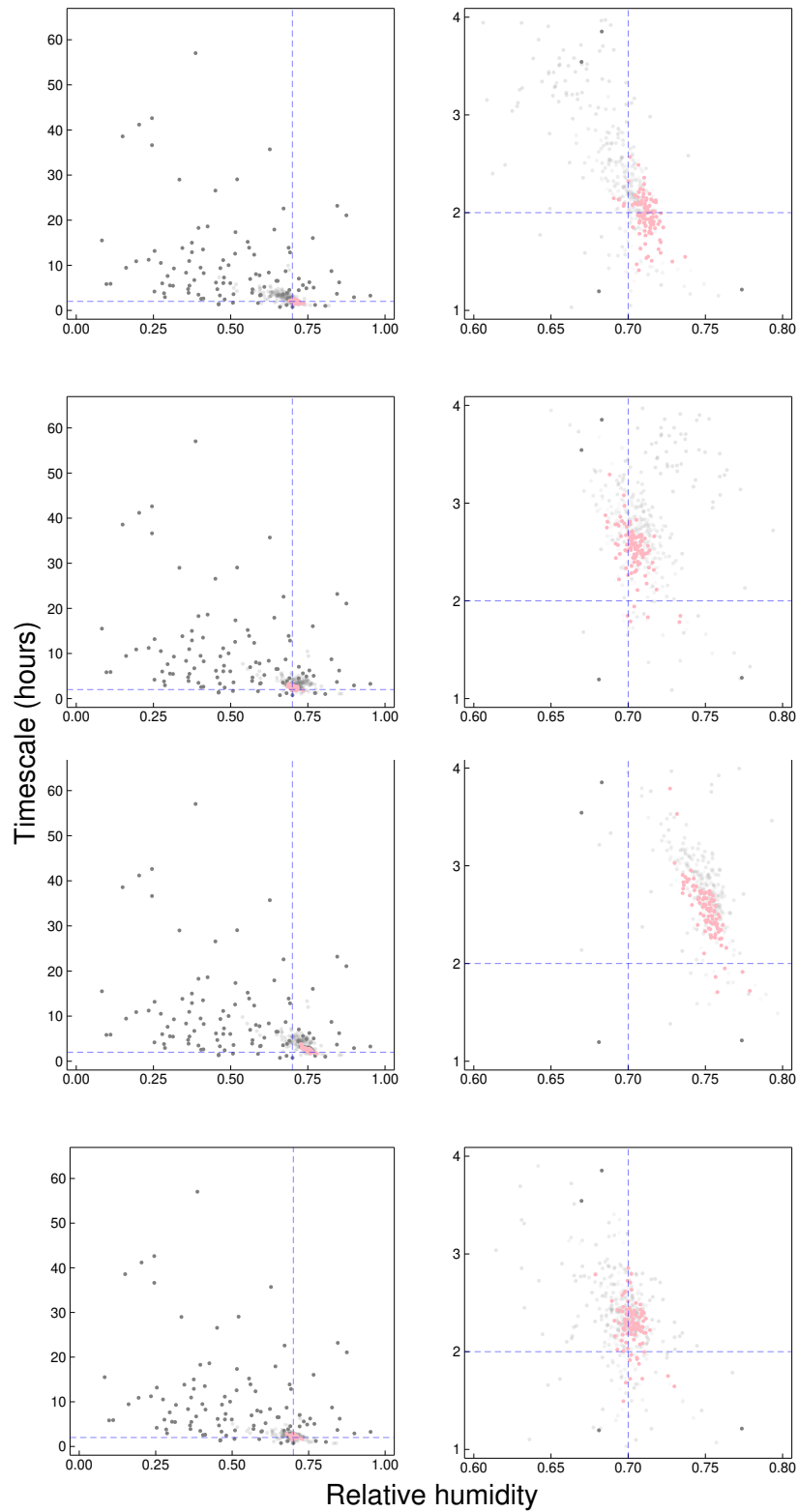


Figure 4. EKI ensemble at iterations 0 to 5 displayed as particles in parameter space. Left column: all members; right column: zoom-in near true parameter values. Each row represents optimization with a different data vector $\mathbf{y}^{(i)}$ from Figure 3. The (initial) prior ensemble 0 is highlighted in dark grey, and the final ensemble 5 is highlighted in pink. The intersection of the dashed blue lines represents the true parameter values used to generate observational data from the GCM.

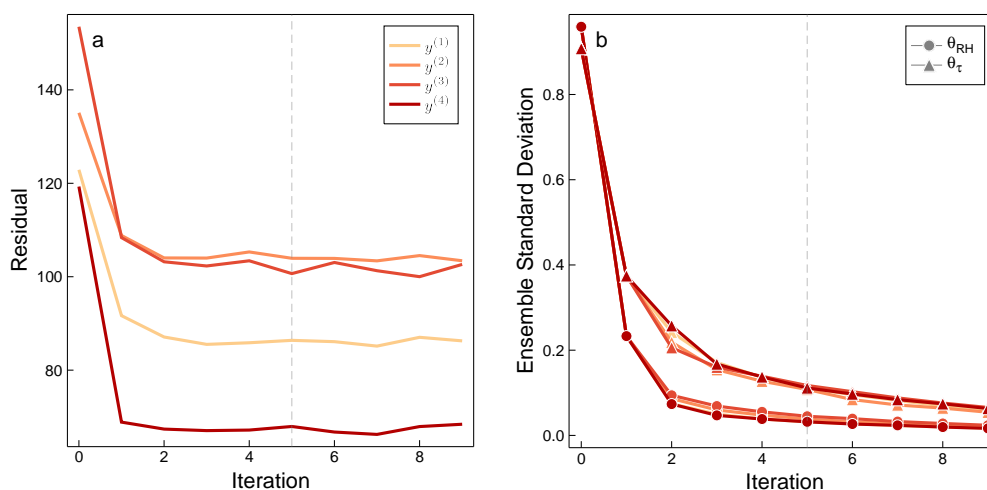


Figure 5. Convergence behaviour tests over 9 iterations of EKI for each realization of the data. The vertical dashed line marks the final iteration of Figure 4; we also show behaviour of 4 further iterations. (a) Ensemble-mean residuals relative to synthetic data for each EKI iteration. (b) Standard deviation of ensemble for the relative humidity parameter (circle) and timescale parameter (triangle) for each realization.

References

633

634 Annan, J. D., & Hargreaves, J. C. (2007). Efficient estimation and ensemble generation in climate modelling. *Phil. Trans. R. Soc. A*, *365*, 2077–2088. doi: 10.1098/rsta.2007.2067

637 Betts, A. K. (1986). A new convective adjustment scheme. Part I: Observational and theoretical basis. *Quart. J. Roy. Meteor. Soc.*, *112*, 677–691.

639 Betts, A. K., & Miller, M. J. (1986). A new convective adjustment scheme. Part II: Single column tests using GATE wave, BOMEX, ATEX and arctic air-mass data sets. *Quart. J. Roy. Meteor. Soc.*, *112*, 693–709.

642 Betts, A. K., & Miller, M. J. (1993). The Betts–Miller scheme. In K. A. Emanuel & D. J. Raymond (Eds.), *The representation of cumulus convection in numerical models* (Vol. 24, pp. 107–121). Am. Meteor. Soc.

645 Bischoff, T., & Schneider, T. (2014). Energetic constraints on the position of the Intertropical Convergence Zone. *J. Climate*, *27*, 4937–4951. doi: 10.1175/JCLI-D-13-00650.1

648 Bony, S., Colman, R., Kattsov, V. M., Allan, R. P., Bretherton, C. S., Dufresne, J.-L., ... Webb, M. J. (2006). How well do we understand and evaluate climate change feedback processes? *J. Climate*, *19*, 3445–3482. doi: 10.1175/JCLI3819.1

652 Bony, S., & Dufresne, J. L. (2005). Marine boundary layer clouds at the heart of tropical cloud feedback uncertainties in climate models. *Geophys. Res. Lett.*, *32*, L20806.

655 Bordoni, S., & Schneider, T. (2008). Monsoons as eddy-mediated regime transitions of the tropical overturning circulation. *Nature Geosci.*, *1*, 515–519. doi: 10.1038/ngeo248

658 Brient, F., & Schneider, T. (2016). Constraints on climate sensitivity from space-based measurements of low-cloud reflection. *J. Climate*, *29*, 5821–5835. doi: 10.1175/JCLI-D-15-0897.1

660 Cess, R. D., Potter, G., Blanchet, J., Boer, G., Ghan, S., Kiehl, J., ... others

661

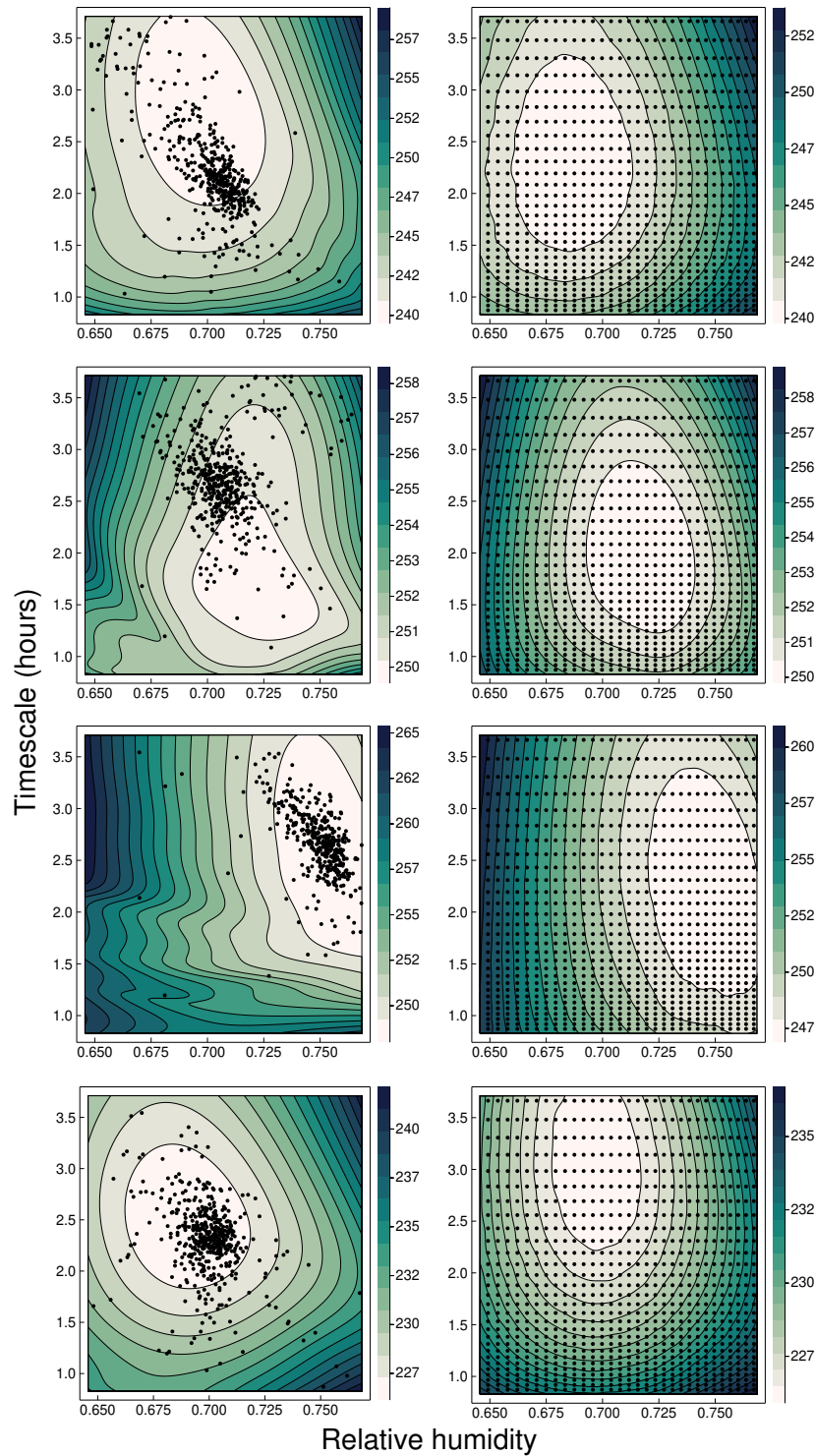


Figure 6. Training points for the GP emulators (EKI-GP and B-GP), plotted over the objective function used in the MCMC algorithm calculated for different realizations $\mathbf{y}^{(1)}, \dots, \mathbf{y}^{(4)}$ of the truth (rows). Left column: particles representing members of the first 6 EKI iterations. Right column: grid (uniform in the transformed parameters) used to train the benchmark Gaussian process. In both cases, some additional training points fall outside of the plotting domain.

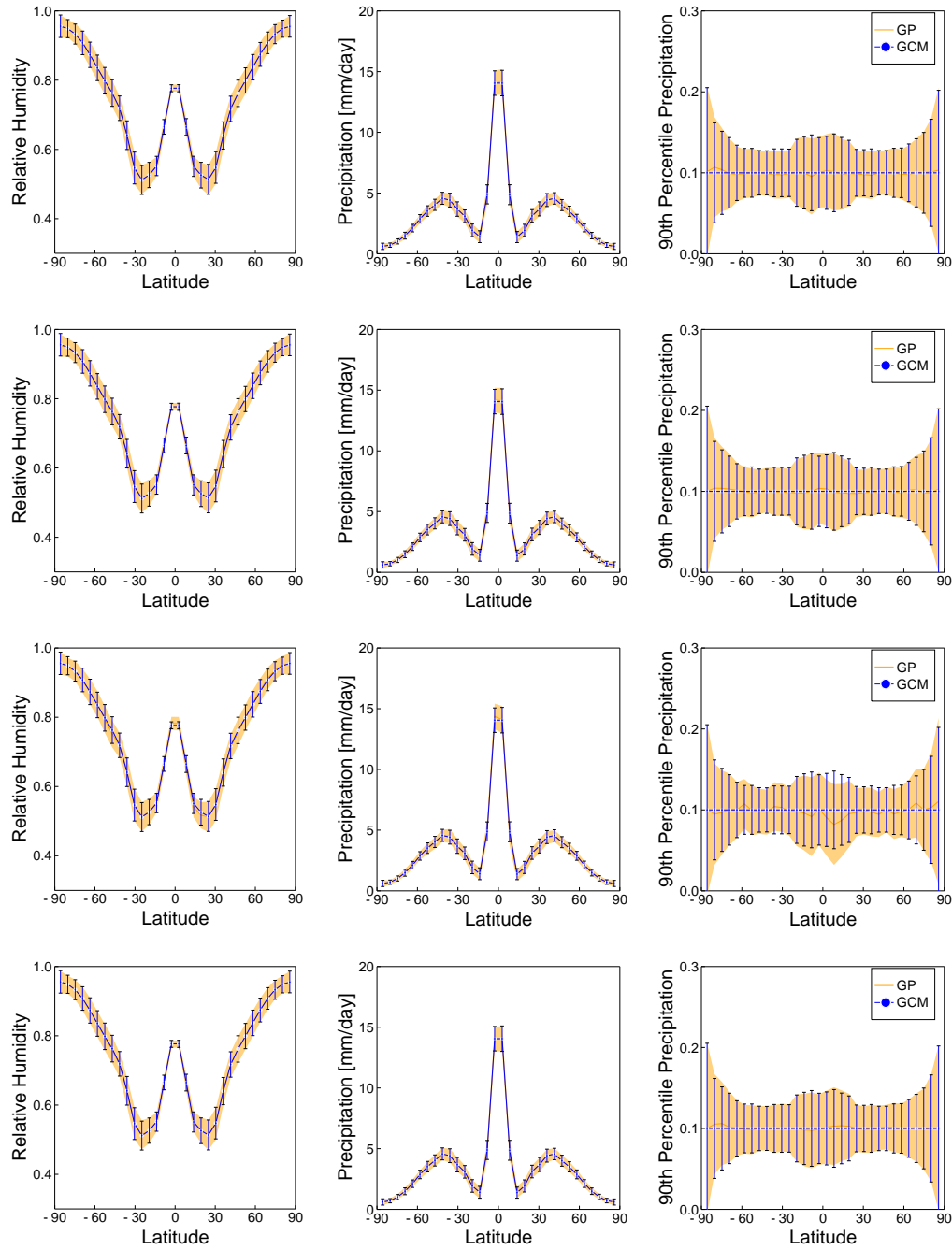


Figure 7. Comparison between the GCM statistics at the true parameters θ^\dagger and the trained EKI-GP emulator at θ^\dagger . The four rows correspond to using EKI against the truths $\mathbf{y}^{(1)}, \dots, \mathbf{y}^{(4)}$. Blue lines: GCM mean (dots) averaged over 600 30-day runs, with the error bars marking a 95% confidence interval from variances on the diagonal of Γ . Orange: predicted mean (line) and 95% confidence interval (shaded region) produced by the GP emulator.

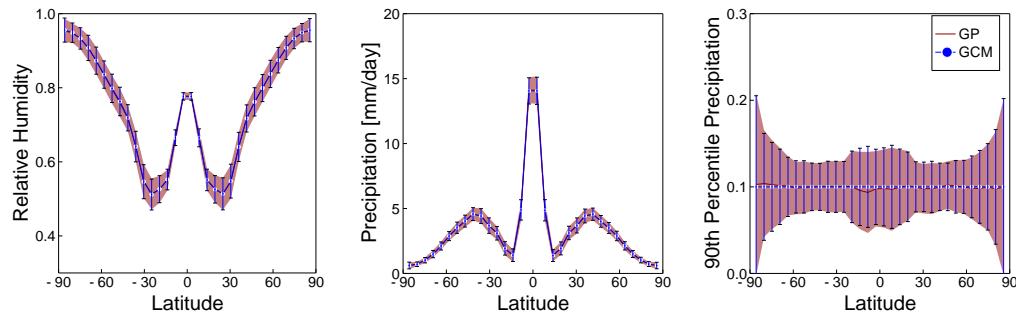


Figure 8. Comparison between the GCM statistics at the true parameters θ^\dagger and the trained B-GP emulator predictions at θ^\dagger . Blue: GCM mean (dots) averaged over 600 30-day runs, with the error bars marking a 95% confidence interval from variances on the diagonal of Γ . Dark red: predicted mean (line) and 95% confidence interval (shaded region) produced by the B-GP emulator.

(1989). Interpretation of cloud-climate feedback as produced by 14 atmospheric general circulation models. *Science*, *245*, 513–516.

Cess, R. D., Potter, G. L., Blanchet, J. P., Boer, G. J., Del Genio, A. D., Déqué, M., ... Zhang, M.-H. (1990). Intercomparison and interpretation of climate feedback processes in 19 atmospheric general circulation models. *J. Geophys. Res.*, *95*, 16601–16615. doi: 10.1029/JD095iD10p16601

Chen, Y., & Oliver, D. S. (2012a). Ensemble randomized maximum likelihood method as an iterative ensemble smoother. *Math. Geosci.*, *44*, 1–26. doi: 10.1007/s11004-011-9376-z

Chen, Y., & Oliver, D. S. (2012b). Ensemble randomized maximum likelihood method as an iterative ensemble smoother. *Mathematical Geosciences*, *44*(1), 1–26.

Cleary, E., Garbuno-Inigo, A., Lan, S., Schneider, T., & Stuart, A. M. (2021). Calibrate, emulate, sample. *J. Comp. Phys.*, *424*, 109716. Retrieved from 10.1016/j.jcp.2020.109716

Couvreux, F., Hourdin, F., Williamson, D., Roehrig, R., Volodina, V., Villefranche, N., ... Xu, W. (2020). Process-based climate model development harnessing machine learning: I. A calibration tool for parameterization improvement. doi: 10.1002/essoar.10503597.1

Edwards, N. R., Cameron, D., & Rougier, J. (2011). Precalibrating an intermediate complexity climate model. *Climate Dynamics*, *37*(7-8), 1469–1482.

Emerick, A. A., & Reynolds, A. C. (2013a). Ensemble smoother with multiple data assimilation. *Computers & Geosciences*, *55*, 3–15.

Emerick, A. A., & Reynolds, A. C. (2013b). Investigation of the sampling performance of ensemble-based methods with a simple reservoir model. *Comp. Geosci.*, *17*, 325–350. doi: 10.1007/s10596-012-9333-z

Ernst, O. G., Sprungk, B., & Starkloff, H.-J. (2015). Analysis of the ensemble and polynomial chaos Kalman filters in Bayesian inverse problems. *SIAM/ASA Journal on Uncertainty Quantification*, *3*(1), 823–851. doi: 10.1137/140981319

Evensen, G. (2018). Analysis of iterative ensemble smoothers for solving inverse problems. *Comp. Geosci.* doi: 10.1007/s10596-018-9731-y

Flato, G., Marotzke, J., Abiodun, B., Braconnot, P., Chou, S. C., Collins, W., ... Rummukainen, M. (2013). Evaluation of climate models. In T. F. Stocker et al. (Eds.), *Climate change 2013: The physical science basis. contribution of*

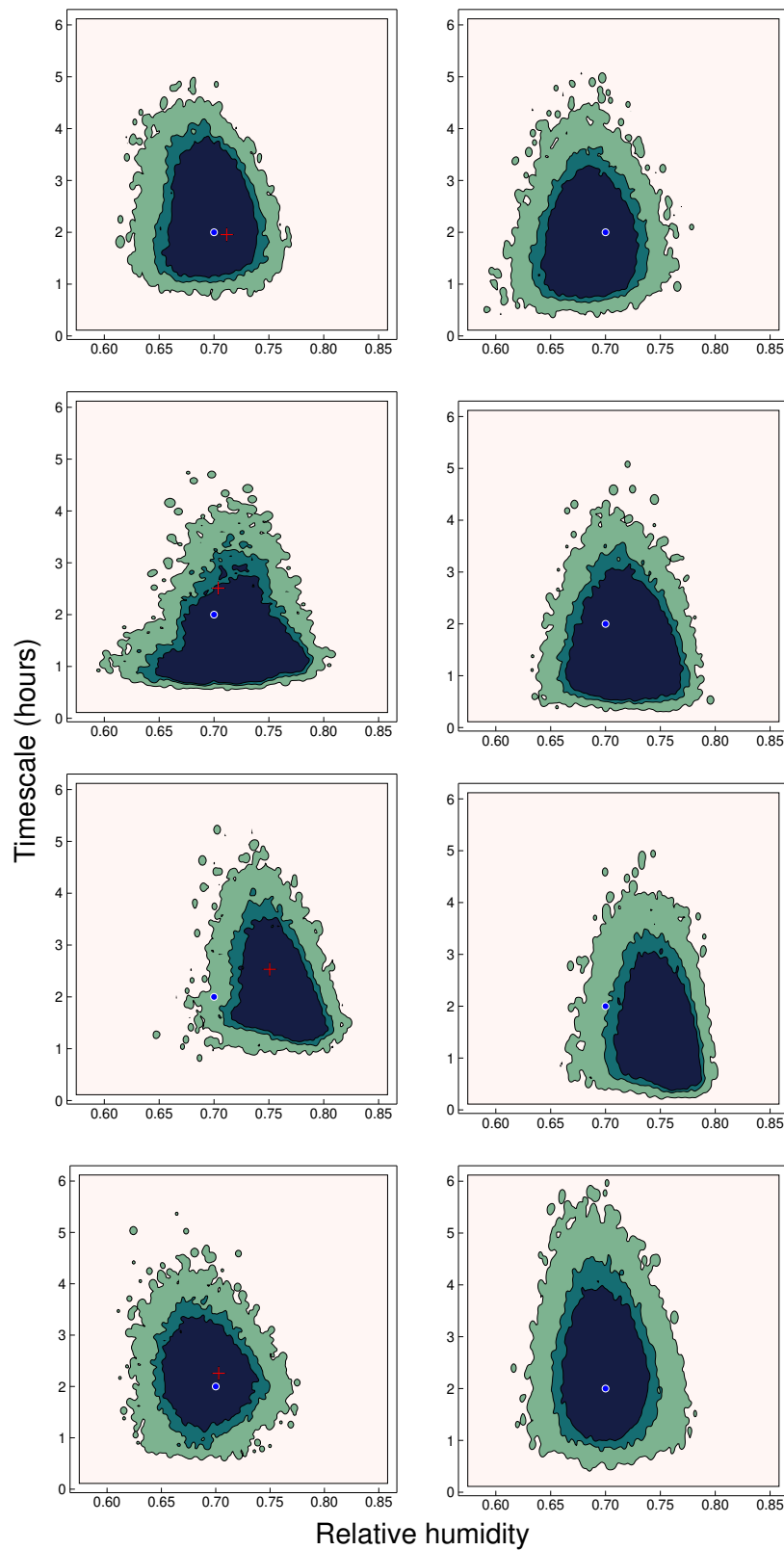


Figure 9. Density plot of MCMC samples of the posterior distribution. The contours are drawn to contain 50%, 75%, and 99% of the distribution generated from the samples. The left column show distributions learned using EKI-GP at $\mathbf{y}^{(1)}, \dots, \mathbf{y}^{(4)}$, and the right column using B-GP at the same realizations. The blue dot represents the true parameters, while the red + is an empirical average of particles in the 6th EKI iteration.

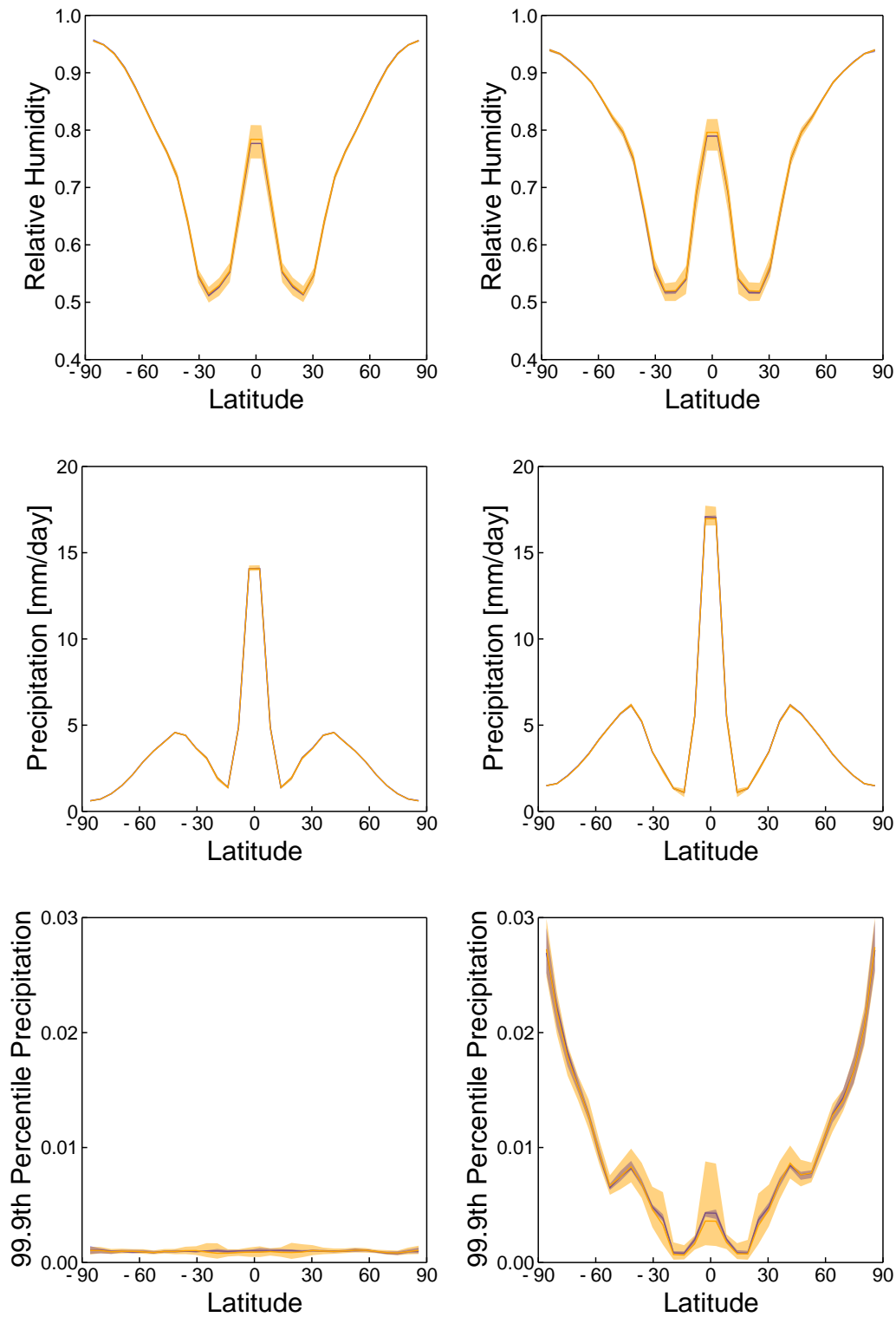


Figure 10. Comparison of statistics of a 7200-day average in a climate-change simulation. Left column: control climate; right column: warmer climate. Synthetic observational data evaluated at the true fixed parameters are shown in blue, while data evaluated at 100 samples from the posterior distribution (EKI-GP) are shown in orange. (We choose the posterior from the first realization of the truth, top-left panel of Figure 9.) The solid lines are the medians, and the shaded regions represent the 95% confidence intervals between the [2.5%, 97.5%] percentiles. Top: Relative humidity in mid-troposphere. Middle: Precipitation rate. Bottom: Frequency with which 99.9th percentile of latitude-dependent daily precipitation in the control climate is exceeded.

- 697 working group i to the fifth assessment report of the intergovernmental panel
 698 on climate change (pp. 741–853). Cambridge, UK, and New York, NY, USA:
 699 Cambridge University Press.
- 700 Frierson, D. M. W. (2007). The dynamics of idealized convection schemes and their
 701 effect on the zonally averaged tropical circulation. *J. Atmos. Sci.*, *64*, 1959–
 702 1976.
- 703 Frierson, D. M. W., Held, I. M., & Zurita-Gotor, P. (2006). A gray-radiation aqua-
 704 planet moist GCM. Part I: Static stability and eddy scale. *J. Atmos. Sci.*, *63*,
 705 2548–2566.
- 706 Garbuno-Inigo, A., Hoffmann, F., Li, W., & Stuart, A. M. (2020). Interact-
 707 ing langevin diffusions: Gradient structure and ensemble Kalman sampler.
 708 *SIAM Journal on Applied Dynamical Systems*, *19*(1), 412–441. Retrieved from
 709 <https://doi.org/10.1137/19M1251655> doi: 10.1137/19M1251655
- 710 Geyer, C. J. (2011). Introduction to Markov Chain Monte Carlo. In S. Brooks,
 711 A. Gelman, G. L. Jones, & X.-L. Meng (Eds.), *Handbook of Markov Chain*
 712 *Monte Carlo*. Chapman and Hall/CRC Press. doi: 10.1201/b10905-3
- 713 Gland, F. L., Monbet, V., & Tran, V.-D. (2009). *Large sample asymptotics for the*
 714 *ensemble kalman filter* (Tech. Rep. No. RR-7014). INRIA.
- 715 Golaz, J.-C., Horowitz, L. W., & II, H. L. (2013). Cloud tuning in a coupled climate
 716 model: Impact on 20th century warming. *Geophys. Res. Lett.*, *40*, 2246–2251.
 717 doi: 10.1002/grl.50232
- 718 Hourdin, F., Grandpeix, J.-Y., Rio, C., Bony, S., Jam, A., Cheruy, F., ... Roehrig,
 719 R. (2013). LMDZ5B: the atmospheric component of the IPSL climate model
 720 with revisited parameterizations for clouds and convection. *Clim. Dyn.*, *40*,
 721 2193–2222. doi: 10.1007/s00382-012-1343-y
- 722 Hourdin, F., Mauritsen, T., Gettelman, A., Golaz, J.-C., Balaji, V., Duan, Q., ...
 723 Williamson, D. (2017). The art and science of climate model tuning. *Bull.*
 724 *Amer. Meteor. Soc.*, *98*, 589–602. doi: 10.1175/BAMS-D-15-00135.1
- 725 Hourdin, F., Williamson, D., Rio, C., Couvreur, F., Roehrig, R., Villefranche,
 726 N., ... Volodina, V. (2020). Process-based climate model develop-
 727 ment harnessing machine learning: II. Model calibration from single col-
 728 umn to global. *Journal of Advances in Modeling Earth Systems*. doi:
 729 <https://doi.org/10.1029/2020MS002225>
- 730 Houtekamer, P. L., & Zhang, F. (2016). Review of the ensemble Kalman filter for
 731 atmospheric data assimilation. *Mon. Wea. Rev.*, *144*, 4489–4532. doi: 10.1175/
 732 MWR-D-15-0440.1
- 733 Iglesias, M. A., Law, K. J. H., & Stuart, A. M. (2013, mar). Ensemble Kalman
 734 methods for inverse problems. *Inverse Problems*, *29*(4), 045001. doi: 10.1088/
 735 0266-5611/29/4/045001
- 736 Järvinen, H., Räisänen, P., Laine, M., Tamminen, J., Ilin, A., Oja, E., ... Haario,
 737 H. (2010). Estimation of ECHAM5 climate model closure paramete-
 738 rters with adaptive MCMC. *Atmos. Chem. Phys.*, *10*, 9993–10002. doi:
 739 10.5194/acp-10-9993-2010
- 740 Kalnay, E. (2002). *Atmospheric modeling, data assimilation and predictability*. Cam-
 741 bridge University Press. doi: 10.1017/CBO9780511802270
- 742 Kalnay, E. (2003). *Atmospheric modeling, data assimilation and predictability*. Cam-
 743 bridge, UK: Cambridge Univ. Press.
- 744 Kaspi, Y., & Schneider, T. (2011). Winter cold of eastern continental boundaries in-
 745 duced by warm ocean waters. *Nature*, *471*, 621–624.
- 746 Kaspi, Y., & Schneider, T. (2013). The role of stationary eddies in shaping midlati-
 747 tude storm tracks. *J. Atmos. Sci.*, *70*, 2596–2613.
- 748 Kennedy, M. C., & O’Hagan, A. (2001). Bayesian calibration of computer models. *J.*
 749 *Roy. Statist. Soc. B*, *63*, 425–464. doi: 10.1111/1467-9868.00294
- 750 Levine, X., & Schneider, T. (2015). Baroclinic eddies and the extent of the Hadley
 751 circulation: An idealized GCM study. *J. Atmos. Sci.*, *72*, 2744–2761. doi: 10

.1175/JAS-D-14-0152.1

752
753 Mauritsen, T., Stevens, B., Roeckner, E., Crueger, T., Esch, M., Giorgetta, M., ...
754 Tomassini, L. (2012). Tuning the climate of a global model. *J. Adv. Model.*
755 *Earth Sys.*, *4*, M00A01. doi: 10.1029/2012MS000154

756 Merlis, T. M., & Schneider, T. (2011). Changes in zonal surface temperature gradi-
757 ents and walker circulations in a wide range of climates. *J. Climate*, *24*, 4757–
758 4768.

759 O’Gorman, P. A. (2011). The effective static stability experienced by eddies in a
760 moist atmosphere. *J. Atmos. Sci.*, *68*, 75–90.

761 O’Gorman, P. A., Lamquin, N., Schneider, T., & Singh, M. S. (2011). The relative
762 humidity in an isentropic advection–condensation model: Limited poleward in-
763 fluence and properties of subtropical minima. *J. Atmos. Sci.*, *68*, 3079–3093.

764 O’Gorman, P. A., & Schneider, T. (2008a). Energy of midlatitude transient eddies
765 in idealized simulations of changed climates. *J. Climate*, *21*, 5797–5806.

766 O’Gorman, P. A., & Schneider, T. (2008b). The hydrological cycle over a wide range
767 of climates simulated with an idealized GCM. *J. Climate*, *21*, 3815–3832.

768 O’Gorman, P. A., & Schneider, T. (2009a). The physical basis for increases in pre-
769 cipitation extremes in simulations of 21st-century climate change. *Proc. Natl.*
770 *Acad. Sci.*, *106*, 14773–14777.

771 O’Gorman, P. A., & Schneider, T. (2009b). Scaling of precipitation extremes over
772 a wide range of climates simulated with an idealized GCM. *J. Climate*, *22*,
773 5676–5685.

774 Oliver, D. S., Reynolds, A. C., & Liu, N. (2008). *Inverse theory for petroleum reser-*
775 *voir characterization and history matching*. Cambridge Univ. Press.

776 Pedregosa, F., Varoquaux, G., Gramfort, A., Michel, V., Thirion, B., Grisel, O., ...
777 Duchesnay, E. (2011). Scikit-learn: Machine learning in Python. *Journal of*
778 *Machine Learning Research*, *12*, 2825–2830.

779 Randall, D. A., & Wielicki, B. A. (1997). Measurements, models, and hypotheses in
780 the atmospheric sciences. *Bull. Amer. Meteor. Soc.*, *78*, 400–406.

781 Roberts, G. O., Rosenthal, J. S., et al. (2004). General state space Markov chains
782 and mcmc algorithms. *Probability surveys*, *1*, 20–71.

783 Sacks, J., Welch, W. J., Mitchell, T. J., & Wynn, H. P. (1989). Design and analysis
784 of computer experiments. *Statistical science*, 409–423.

785 Santner, T. J., Williams, B. J., Notz, W., & Williams, B. J. (2018). *The design and*
786 *analysis of computer experiments* (2nd ed.). New York, NY: Springer.

787 Schillings, C., & Stuart, A. M. (2017). Analysis of the ensemble kalman fil-
788 ter for inverse problems. *SIAM Journal on Numerical Analysis*, *55*(3),
789 1264–1290. Retrieved from <https://doi.org/10.1137/16M105959X> doi:
790 10.1137/16M105959X

791 Schirber, S., Klocke, D., Pincus, R., Quaas, J., & Anderson, J. L. (2013, mar).
792 Parameter estimation using data assimilation in an atmospheric general circula-
793 tion model: From a perfect toward the real world. *Journal of Advances in*
794 *Modeling Earth Systems*, *5*(1), 58–70. doi: 10.1029/2012MS000167

795 Schmidt, G. A., Bader, D., Donner, L. J., Elsaesser, G. S., Golaz, J.-C., Hannay,
796 C., ... Saha, S. (2017). Practice and philosophy of climate model tuning
797 across six u.s. modeling centers. *Geosci. Model Dev.*, *10*, 3207–3223. doi:
798 10.5194/gmd-2017-30

799 Schneider, T., Lan, S., Stuart, A., & Teixeira, J. (2017). Earth system model-
800 ing 2.0: A blueprint for models that learn from observations and targeted
801 high-resolution simulations. *Geophys. Res. Lett.*, *44*, 12396–12417. doi:
802 10.1002/2017GL076101

803 Schneider, T., & O’Gorman, P. A. (2008). Moist convection and the thermal stratifi-
804 cation of the extratropical troposphere. *J. Atmos. Sci.*, *65*, 3571–3583.

805 Schneider, T., O’Gorman, P. A., & Levine, X. J. (2010). Water vapor
806 and the dynamics of climate changes. *Rev. Geophys.*, *48*, RG3001.

- (doi:10.1029/2009RG000302)
- 807 Schneider, T., Stuart, A. M., & Wu, J.-L. (2020a). Ensemble Kalman inversion for
808 sparse learning of dynamical systems from time-averaged data. *arXiv preprint*,
809 *arXiv:2007.06175*.
- 810
811 Schneider, T., Stuart, A. M., & Wu, J.-L. (2020b). Learning stochastic closures us-
812 ing ensemble Kalman inversion. *arXiv preprint*, *arXiv:2004.08376*.
- 813 Schneider, T., Teixeira, J., Bretherton, C. S., Brient, F., Pressel, K. G., Schär, C.,
814 & Siebesma, A. P. (2017). Climate goals and computing the future of clouds.
815 *Nature Climate Change*, *7*, 3–5. doi: 10.1038/nclimate3190
- 816 Solonen, A., Ollinaho, P., Laine, M., Haario, H., Tamminen, J., & Järvinen, H.
817 (2012). Efficient mcmc for climate model parameter estimation: Parallel
818 adaptive chains and early rejection. *Bayesian Analysis*, *7*(3), 715–736. doi:
819 10.1214/12-BA724
- 820 Stephens, G. L. (2005). Cloud feedbacks in the climate system: A critical review. *J.*
821 *Climate*, *18*, 237–273. doi: 10.1175/JCLI-3243.1
- 822 Vernon, I., Goldstein, M., & Bower, R. G. (2010, 12). Galaxy formation: A
823 Bayesian uncertainty analysis. *Bayesian Analysis*, *5*(4), 619–669. doi:
824 10.1214/10-BA524
- 825 Vial, J., Dufresne, J.-L., & Bony, S. (2013). On the interpretation of inter-model
826 spread in CMIP5 climate sensitivity estimates. *Clim. Dyn.*, *41*, 3339–3362. doi:
827 10.1007/s00382-013-1725-9
- 828 Webb, M. J., Lambert, F. H., & Gregory, J. M. (2013). Origins of differences in cli-
829 mate sensitivity, forcing and feedback in climate models. *Clim. Dyn.*, *40*, 677–
830 707. doi: 10.1007/s00382-012-1336-x
- 831 Wei, H.-H., & Bordoni, S. (2018). Energetic constraints on the ITCZ position in ide-
832 alized simulations with a seasonal cycle. *J. Adv. Model. Earth Sys.*, *10*. doi: 10
833 .1029/2018MS001313
- 834 Williamson, D., Goldstein, M., Allison, L., Blaker, A., Challenor, P., Jackson, L.,
835 & Yamazaki, K. (2013). History matching for exploring and reducing cli-
836 mate model parameter space using observations and a large perturbed physics
837 ensemble. *Climate dynamics*, *41*(7-8), 1703–1729.
- 838 Wills, R. C., Levine, X. J., & Schneider, T. (2017). Local energetic constraints on
839 Walker circulation strength. *J. Atmos. Sci.*, *74*, 1907–1922. doi: 10.1175/JAS
840 -D-16-0219.1
- 841 Zhao, M., Golaz, J.-C., Held, I. M., Guo, H., Balaji, V., Benson, R., ... Xiang,
842 B. (2018). The GFDL global atmosphere and land model AM4.0/LM4.0: 2.
843 Model description, sensitivity studies, and tuning strategies. *J. Adv. Model.*
844 *Earth Sys.*, *10*, 735–769. doi: 10.1002/2017MS001209